Geophysical Journal International

Geophys. J. Int. (2025) **243,** 1–19 https://doi.org/10.1093/gji/ggaf307
Advance Access publication 2025 August 11
Research Paper

Induced polarization of volcanic rocks. 9. Anatomy of a rising thermal plume

L. Piolat,[1] A. Revil,[2] P. Cosme,[1] Y. Géraud,[1] T. Dupaigne,[3] W. Wheeler,[4] J. Tveranger,[4] B. Lønøy,[4] E. Turinimana,[5] E. Karangwa[5] and A. Favier[1]

[1] *Université de Lorraine, CNRS, GeoRessources, F-54000 Nancy, France. E-mails: loris.piolat@univ-lorraine.fr, pierre.cosme@univ-lorraine.fr, yves.geraud@univ-lorraine.fr, alexiane.favier@univ-lorraine.fr*
[2] *Université Savoie Mont-Blanc, CNRS, UMR CNRS 5204, EDYTEM, 73370 Le Bourget du Lac, France. E-mail: andre.revil@univ-smb.fr*
[3] *WGS, 93500 Pantin, France. E-mail: timothee.dupaigne@wgs-france.com*
[4] *NORCE Norwegian Research Centre, 5008 Bergen, Norway. E-mails: walter.wheeler@norceresearch.no, jan.tveranger@norceresearch.no, bjarte.lonoy@norceresearch.no*
[5] *EDCL, Energy Development Corporation Limited, Kigali, Rwanda. E-mails: eturinimana@edcl.reg.rw, eukarangwa@edcl.reg.rw*

Accepted 2025 August 7. Received 2025 August 6; in original form 2025 April 16

SUMMARY

The dynamic Stern layer petrophysical model can be used to interpret field induced polarization data and can be applied to both magmatic (volcanic and igneous) rocks and sediments. Thanks to it, field-scale tomograms of conductivity and normalized chargeability can be transformed into tomograms of porosity, Cation Exchange Capacity (CEC) and temperature. Furthermore, kilometer-scale galvanometric induced-polarization surveys are nowadays doable thanks to the recent development of independent stations measuring the primary and secondary electrical fields. This approach reduces capacitive and inductive coupling effects inherent to systems based on long cables and allow for deeper investigations. We apply here this combined methodology (novel equipment and revised petrophysical model) to a geothermal prospect located at Mashyuza, Republic of Rwanda, in Eastern Africa. At this site, the rifting activity led to the occurrence of an extensional regime favouring the occurrence of a rising thermal plume at the intersection between two faults. The existence of this plume is expressed at the ground surface by the presence of a hot spring at a temperature of $\sim$52 °C (a well nearby provides a temperature of $\sim$65 °C). A time-domain large-scale induced polarization survey is performed. The current source signal is produced by a VIP-5000 squared signal injector and injection current values range from 1 to 4 A, with stacking of 1 s on–off signals ranging from 100 to 300 stacks to improve the signal-to-noise ratio. The size of the 3-D array is $\sim$1.5 km and allows a tomography down to a depth of $\sim$300 m. The data are inverted with the deterministic least-square technique, penalizing the roughness of the resulting tomograms. The conductivity and normalized chargeability tomograms are combined to get the temperature, porosity and CEC distributions. The temperature distribution is consistent with the temperature of the hot spring and well. The results are interpreted in terms of ground water flow pattern and dilution of the mineralized thermal water with the fresher surface meteoric water. The survey images a rising plume of warm water from a depth of at least 300 m along intersecting fracture systems.

Key words: Electrical properties; Electrical resistivity tomography (ERT); Tomography; Hydrothermal systems; Africa; Hotspots.

1 INTRODUCTION

Since the beginning of the industrial revolution, the widespread use of fossil-based energy sources has led to the observed anthropic climate change (Frisken 1971). In the current context of ecological transition, the development of renewable energies is now mandatory for maintaining the worldwide energy production (e.g. Schiermeier 2013; Ergen & Sucker 2021) while reducing greenhouses gases emissions. In this context, geothermal energy is a suitable energy source (Nkinyam *et al.* 2025) for direct-use of calorific energy or electricity generation.

Until now, geothermal exploration was mostly based on electrical resistivity exploration (galvanometric or induction-based) to analyse geothermal systems and understand their ground water flow

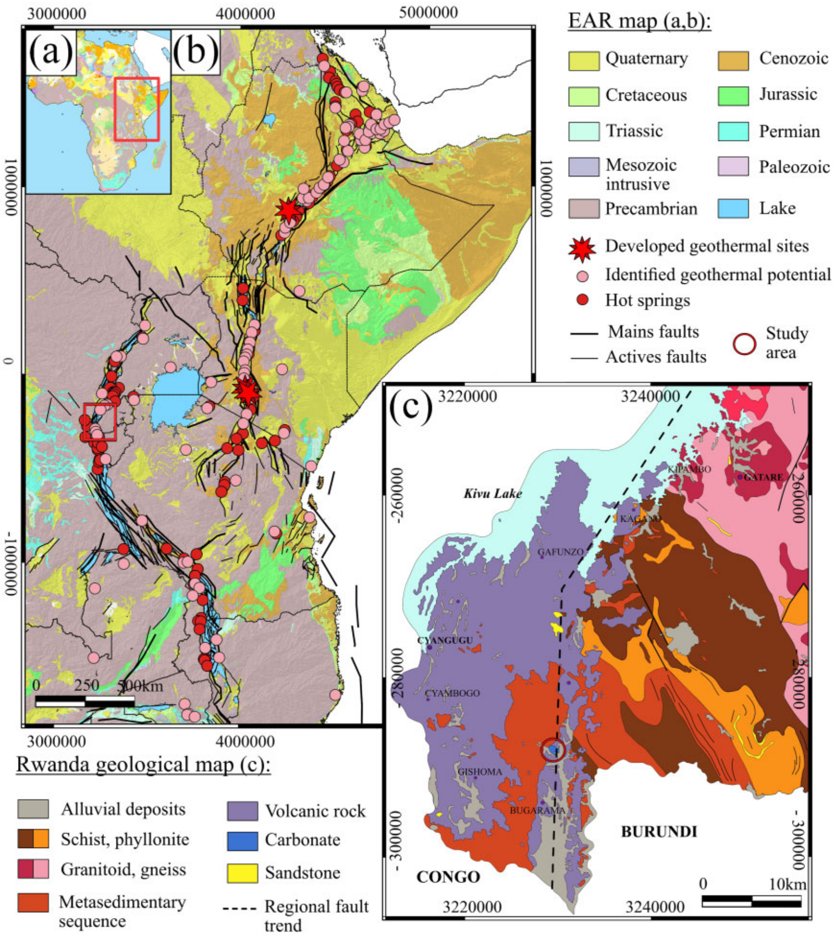

Figure 1. Regional geological context of the survey. (**a**) Map of Africa. (**b**) Location of the East African Rift (EAR) at the continental scale, showing the major geological, structural and geothermal potential features. The maps were created using Qgis software and based on regional geospatial data from the RCMRD (Regional Center for Mapping of Resources for Development). Tectonic and geological information from the USGS (United States Geological Survey), as well as geothermal and energy data from the BGS (British Geological Survey) and the Africa Knowledge Platform. The base map and visual elements were adapted from the UNESCO Digital Library. The hot spring known as Amashyuza is located in the western branch of the EAR area on the east side of the Kivu Lake. (**c**) Simplified geological map of western Rwanda (scale 1:250 000) showing main lithological units. Produced as part of a Belgian Development Cooperation project by the National Geographic Institute of Belgium and Rwandan Republic Natural Resources Ministry (1981), and available online via the European Soil Data Center (ESDAC). The filled circle is pointed on the location of the test site.

pattern (e.g. Muñoz *et al.* 2010a b; Navelot *et al.* 2018; Gresse *et al.* 2021). Electrical resistivity can be obtained by either galvanometric or induction based electromagnetic techniques (Finizola *et al.* 2006; Muñoz 2014). Unfortunately, the resistivity of rocks is at least controlled by the following two factors. One of them is related to conduction of the electrical current in the pore network of a rock and is based on Archie's law (Archie 1942). A second contribution is called surface conductivity and is associated with the conduction in the electrical double layer coating the surface of the minerals (see Flóvenz 2005 for volcanic rocks and Waxman & Smits 1968 for sedimentary rocks). This double layer comprises the Stern and Gouy-Chapman layers on the surface of the minerals forming the skeleton of a porous body. This second contribution is controlled by the Cation Exchange Capacity (CEC) of the material, especially when clay minerals are produced in response to the alteration of the primary minerals of silicate rocks (e.g. Fulignati 2020; and references therein). Because of this complexity, numerous authors have neglected surface conductivity assuming *ipse facto* that Archie's law governs electrical conductivity (e.g. Li *et al*. 2025). Unfortunately, the opposite was proven to be true, that is, surface conductivity dominates the conductivity of the volcanic rocks in most, if not all, cases (Flóvenz 2005; Revil *et al.* 2017a, 2019) There are however some exceptions for instance related to very ionic strength and acidic pore waters associated with strato-volcanoes as recently outlined by Revil *et al.* (2022).

Induced polarization is a galvanometric method that can be used in the field with the same equipment and in the same timeframe than electrical resistivity tomography (e.g. Flores Orozco *et al.* 2020; Glaser 2021; Glaser *et al.* 2021, 2023; Koohbor *et al.* 2022). In the recent few years, it has been heavily developed to solve hydrogeophysical problems including those associated with environmental issues (*e.g.* Ntarlagiannis *et al.* 2010; Flores Orozco *et al.* 2011; Martin 2012; Martin *et al.* 2015; Mellage *et al.* 2018; Ma *et al.* 2025). Induced polarization measures the ability of rocks and sediments to reversibly store electrical charge carriers under an applied, low-frequency, electrical field (e.g. Olhoeft 1981a, b; Lesmes & Frye 2001; Weller & Slater 2015). Such low-frequency (<10 kHz) polarization mechanisms are essentially due to the polarization of the electrical double layer coating the surface of the grains (e.g. Dias 1972; Dukhin & Shilov 1974; Fixman 1980; Börner & Schön

Figure 2. Pictures of the test site. (**a**) Picture of the main hot spring (Measurements sites 3–4-8, see Table 1). (**b**) Picture of the main resurgence (Measurement site 5, Table 1) and travertine quarry. (**c**) Metasediment outcrop. (**d**) Basalt outcrop.

1991). The reversible storage of electrical charge carriers is characterized by a rock property called the normalized chargeability (and quadrature conductivity) of porous rocks. Additional mechanisms are now well-understood as the polarization associated with the electrodiffusion of the p-holes and electrons in semiconductors (Revil *et al.* 2015a, b) or controlled by electro-redox reactions on the surface of these materials (Wong 1979).

Since the surface conductivity of volcanic rocks is proportional to their normalized chargeability, induced polarization can be used to remove the above-mentioned difficulty in interpreting field resistivity measurements, that is, separating the surface and bulk conductivity components which cannot be achieved with resistivity alone (Revil *et al.* 2017a, , 2019). Revil *et al.* (2017a, have developed a mechanistic petrophysical model called the Dynamic Stern Layer (DSL) model and explained how the induced polarization properties of volcanic rocks result from the polarization of the electrical double layer of clay minerals. This model was successfully applied in the previous papers of this series to various types of rocks resulting from various types of magmatic activity including shield volcanoes (Revil *et al.* 2021), stratovolcanoes (Zhang *et al.* 2023), kimberlites (Titov *et al.* 2024) and igneous granitic rocks (Piolat *et al.* 2025). The previous works in this series have successfully demonstrated the use of the DSL model in the realm of geothermal systems and volcanoes (see a review in Revil & Gresse 2021). This paper aims to proof-test and show-case this methodology in the case of large field investigations with the newly developed distributed acquisition system by IRIS called the FullWaver System®. The case study of thermal plume imaging described in this paper is also unique because carbonate precipitation is also present in the system, which alters significantly the interfacial properties of volcanic rocks and metasediments.

The field experiment reported herein occurred under the auspices of the LEAP-RE (for Long-term joint European union-African union research and innovation Partnership on Renewable Energy) programme. This programme has been developed to trigger the development of innovative actions towards renewable energy development in African countries, and among them geothermal energy. The Geothermal Village project was awarded by the LEAP-RE grant and focuses on developing geothermal energy in the EAR (East African Rift) areas where major untapped geothermal resources have been identified over the last decades. The EAR system is one of the largest active tectonic zones on Earth. It is formed through a set of extensional basins and volcanic formations (Girdler *et al.* 1969; Chorowicz 2005). These two main characteristics explain how the EAR hosts hundreds of identified geothermal potential areas along thousands of kilometers of extensional faults. Extensional strain

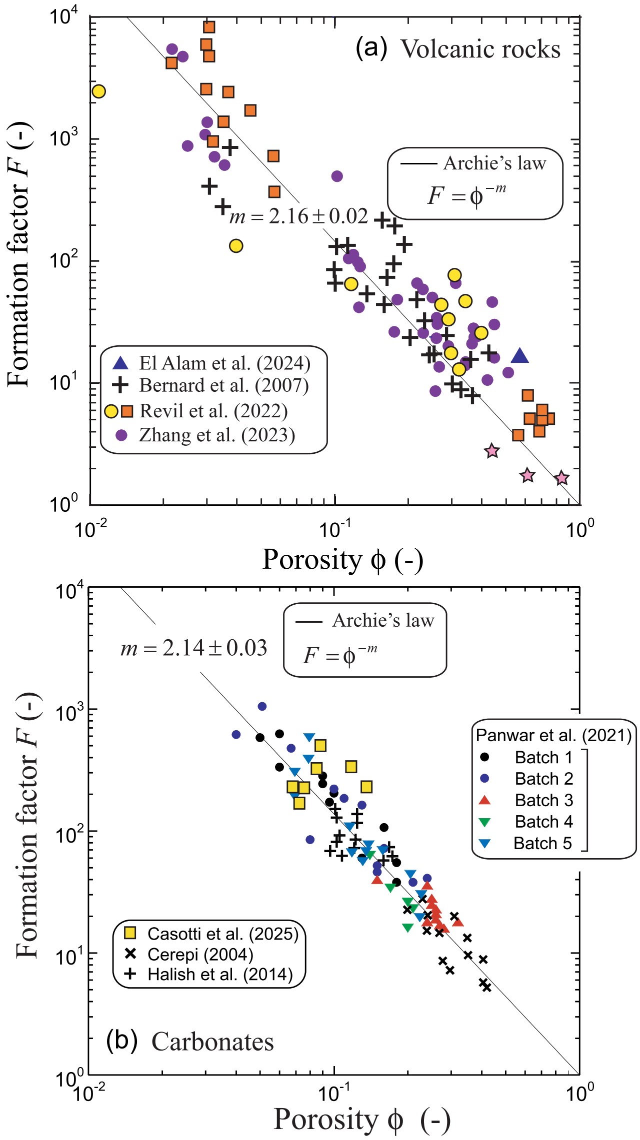

Figure 3. Intrinsic formation factor versus porosity and fit with Archie's law. (**a**) Volcanic rocks with data from El Alam *et al.* (2024) (end member smectite-rich), Bernard *et al.* (2007), Revil *et al.* (2022) and Zhang *et al.* (2023). (**b**) Carbonate rocks. Data from Panwar *et al.* (2021), Halisch *et al.* (2014) and Cerepi (2004). Note the very similar value for the cementation exponent *m*.

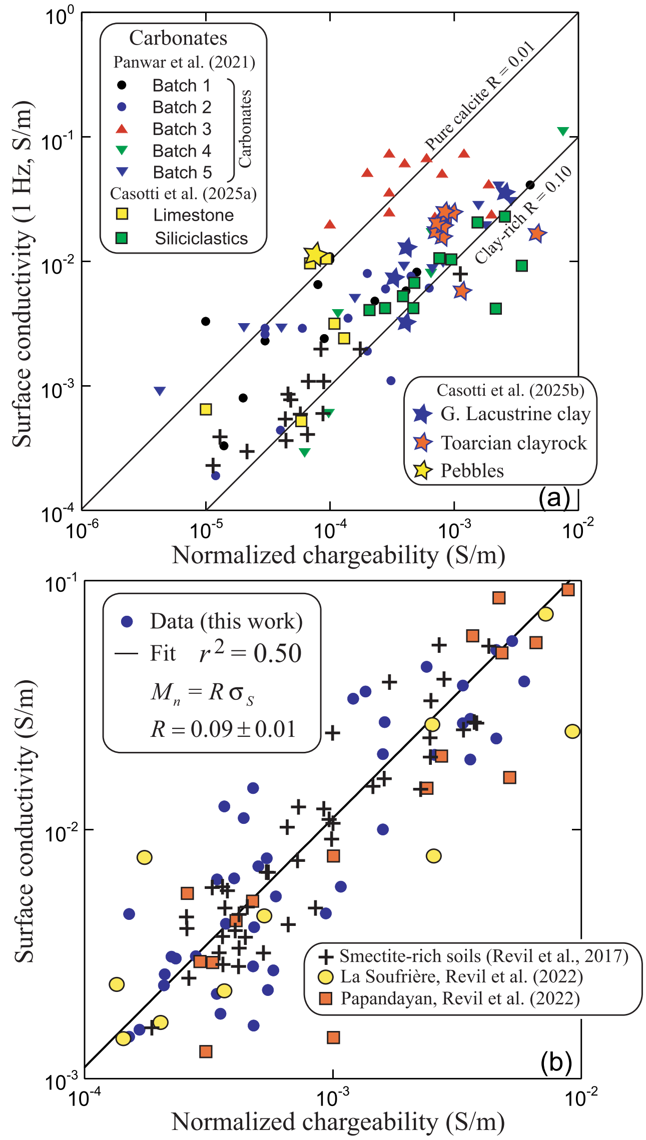

Figure 4. Comparison between surface conductivity and normalized chargeability. (**a**) The ratio between the two quantities defines the value of the dimensionless number R (= 0.10 for clay minerals, see Revil *et al.* 2017b). The data reported in Casotti *et al.* (2025a, b) correspond to shallow sedimentary rocks. (**b**) Volcanic rocks.

and volcanic activity are not evenly distributed and develop different geothermal plays depending on the local geological context. So far, these resources have been however insufficiently characterized and new efforts are currently underway to better document the potential of some of these areas (see for instance Piolat *et al.* 2023).

The hot spring site known as Mashyuza in Kinyarwanda is located in the Western branch of EAR, named the Kivu Rift, on the east side of Lake Kivu (see Figs 1 and 2). The Mashyuza test site is located in the Nyakabuye district, 5 km North of the city of Bugarama and one kilometer west of the Rubyiro river, in the Bugarama graben, that is one of the southeastern structure of the Kivu Rift (Ebinger 1989). The rifting, in this area, is active since the Miocene (Michon *et al.* 2022) and is closely associated with two interacting main fault systems (with NE–SW and NNE–SSW trends) and a newly formed N–S fault. These faults are inherited of the Mesoproterozoic Karagwe–Ankole belt (Villeneuve 1978; Villeneuve & Chorowicz 2004). In the area of interest, the faults cross two formations of the Bugarama group. The oldest one is the Kashenie formation, few hundred meters thick, composed by micashists and calc-micashists with porphyroblasts of garnet, biotite and magnetite. It is overlayed by the Kamanyola formation (2300 m thick), that is composed of interbedded quartzite, metapelites, quartzo-pelites with intercalated amphibolitic sills. These formations are affected by a greenschist facies metamorphism acquired during two strain phases, associated to fold and thrust development. The associated schistosity presents a paragenesis with quartz, biotite, muscovite, sericite, garnet and tourmaline (Rwandan Republic Natural Resources Ministry 1981; Ebinger 1989; Villeneuve *et al.* 2019). The faulting activity is preceded by tholeiitic lava flows, with olivine and clinopyroxene phenocrysts an in intergranular matrix of plagioclase, olivines

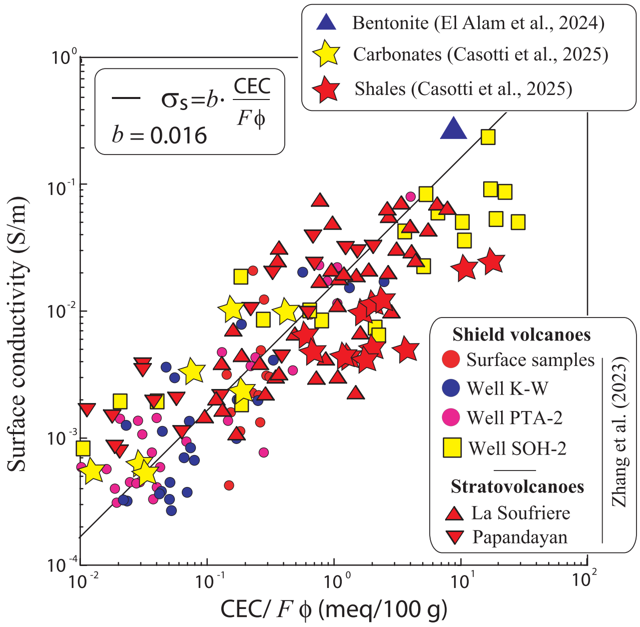

Figure 5. Surface conductivity versus the normalized CEC defined as the CEC divided by the tortuosity of the pore space (product of the formation factor by the connected porosity). The data set comprises volcanic rocks from shield and stratovolcanoes (Zhang *et al.* 2023), bentonite (El Alam *et al.* 2025) and the data from Casotti *et al.* (2025a, b) carbonates, sandstones and shales). This figure has been updated from the study of Zhang *et al.* (2023) by adding the end-member case (smectite-rich) from the study of El Alam *et al.* 2025) and the data from Casotti *et al.* (2025a, b) for carbonates.

clino- and orthopyroxene (Pasteels *et al.* 1989; Pouclet *et al.* 2016) and dated between 11.4 and 9 Ma (Pasteels *et al.* 1989; Kampuzu *et al.* 1998; Pouclet et al 2016) (see Fig. 1c). The valley bottom is filled by recent alluvial and fluvial deposits in the hydrographical network.

On-site, travertines precipitate due to the upflow of thermal mineralized ground waters along a fracture network as described by travitonics concepts (Hancock *et al.* 1999; Brogi *et al.* 2021) (Fig. 1c). These hot springs have been known and used for centuries for their healing properties. Locals often visit them to seek both physical and spiritual relief and, as a consequence, the Mashyuza springs have come to be associated with cleansing rituals in the local culture. Our goal is to use deep resistivity and induced polarization signals to better characterize the rising thermal plume associated with this hot spring and to obtain a temperature tomography of the area using the approach developed in the previous papers of this series.

2 PETROPHYSICAL MODEL

The development of a consistent petrophysical model for both the electrical conductivity and normalized chargeability of rocks was achieved in a set of papers by Revil (2013) and Revil *et al.* (2017a,) based on previous works by Waxman & Smits (1968) and Vinegar & Waxman (1984). We assume that there are no semiconductors in the formations. The presence of pyrite or magnetite above 1 per cent of volumetric content is known to contribute to a strong induced polarization component in addition to the clay polarization mentioned above (Wong 1979; Gurin *et al.* 2015, 2019; Günther & Martin 2016). The polarization is here associated with the existence of the electrical double layer surrounding the mineral grains (e.g. Bücker *et al.* 2019). In their simplest form and for water-saturated porous media, we have the following expressions for the conductivity and normalized chargeability (Revil 2012, 2013; Revil *et al.* 2013; Revil *et al.* 2017b),

$$\sigma \approx \frac{1}{F}\sigma_w + \frac{1}{F\phi}\rho_g B \,\mathrm{CEC}, \tag{1}$$

$$M_n = \frac{1}{F\phi}\lambda\rho_g \mathrm{CEC}, \tag{2}$$

where the formation factor F (dimensionless) is related to the connected porosity (dimensionless) by Archie's law (Archie 1942),

$$F \approx \phi^{-m}, \tag{3}$$

where $m > 1$ denotes the so-called porosity (cementation) exponent (dimensionless).

The CEC denotes the Cation Exchange Capacity (usually expressed in meq/100 g where meq means milliequivalent moles of surface electrical charges or expressed in C kg^{-1}, the conversion being 1 meq/100 g = 963.20 C kg^{-1}). The CEC represents the excess (surface) electrical charge per unit mass of clay minerals. It is traditionally measured with the methylene blue and the cobalt hexamine methods (e.g. Aran *et al.* 2008). In eqs (1) and (2), σ_w (S m^{-1}) denotes the conductivity of the pore water, which depends on both temperature and salinity. The quantity ρ_g (kg m^{-3}) denotes the grain density, and B and λ (both in m^2 s^{-1} V^{-1}) denotes two effective ionic mobilities for conduction and polarization (B(Na$^+$, 25 °C) = 3.1 × 10^{-9} m^2 s^{-1} V^{-1} and λ(Na$^+$, 25 °C) = 3.0 × 10^{-10} m^2 s^{-1} V^{-1}). In our paper, we neglect the small salinity effect on the quadrature conductivity (alternatively on the normalized chargeability, see Weller *et al.* (2011) and Revil & Skold (2011), for a discussion regarding this effect).

In the field survey discussed below, we are dealing with both silicate and carbonate lithofacies. To validate the applicability of the method used below (confirmed in a series of prior studies) three key points need to be addressed: (i) the value of the porosity (cementation) exponent m for basaltic and carbonate rocks, (ii) the dependence of surface conductivity (the last term of eq. 1) with the CEC and (iii) the proportionality between the normalized chargeability and the surface conductivity since from eqs (1) and (2), we have (see Panwar *et al.* 2021; Zhang *et al.* 2023),

$$\frac{M_n}{\sigma_S} = \frac{\lambda}{B} = R, \tag{4}$$

where $\sigma_S = \rho_g B\mathrm{CEC}/F\phi$ defined the (instantaneous) surface conductivity, and where the dimensionless parameter R is equal to 0.010 ± 0.005 for carbonate rocks (Panwar *et al.* 2021) and 0.10 ± 0.02 for volcanic rocks (Revil & Gresse 2021; Revil *et al.* 2021, 2022). In these equations, R is independent of both the water content and temperature (Revil *et al.* 2017b). Using values reported in the literature, Figs 3–5 validates the DSL model. Fig. 3 shows Archie's law $F = \phi^{-m}$ between the (intrinsic) formation factor F and the (connected) porosity ϕ. We use literature data for both volcanic rocks and carbonates, the two lithologies present at the test site. Fig. 3 shows that for both lithologies, the porosity (cementation) exponent is given by $m \approx 2.1 \pm 0.1$. Similarly, Fig. 4 shows that the surface conductivity is proportional to the normalized chargeability of porous rocks with distinct values of R for carbonates and volcanic rocks. Finally, the relationship between the surface conductivity and the normalized CEC (CEC divided by the product of the formation factor by the connected porosity) is tested in Fig. 5. This figure has been updated from the study of Zhang *et al.* (2023) by adding the end-member case (smectite-rich) from the study of El Alam *et al.*

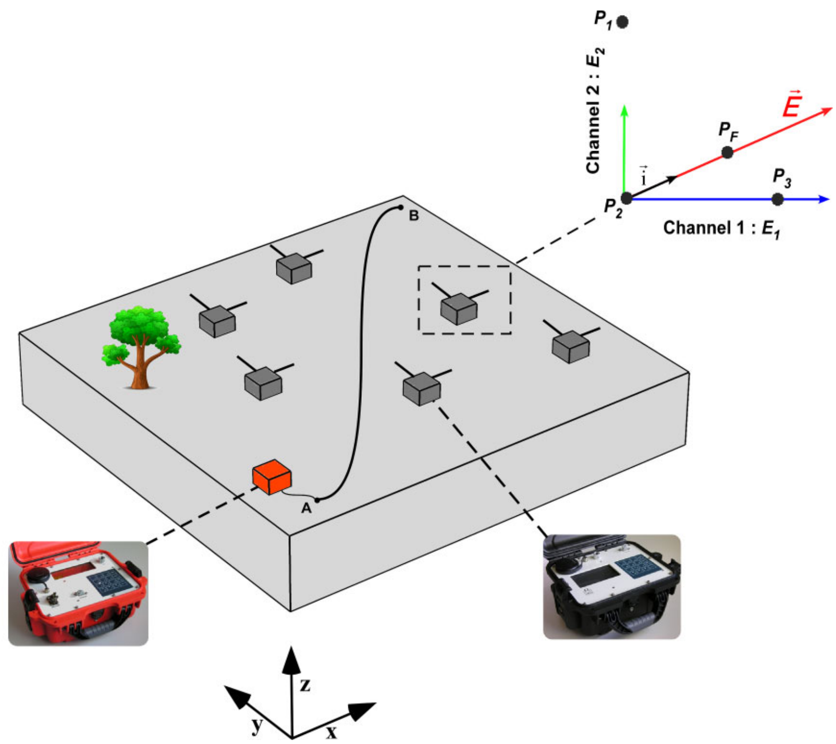

Figure 6. Large-scale time-domain induced polarization measurements with independent stations. The system is composed of an emitter that inject periodic square currents in the ground between electrodes A (fixed) and B (mobile). The recording system is formed by a set of independent stations recording the two components of the electrical field **E** along two dipoles P_1P_2 and P_1P_3. The electrical field recorded during the current injection is called the primary electrical field and is used to determine the conductivity distribution of the surbsurface. The electrical field measured after shutting down the current between A and B is called the secondary electrical field and is used to image the chargeability of the subsurface. Once the tomograms of the conductivity (expressed in S m^{-1}) and chargeability (unitless, mV $\mathrm{V}^{-1} = 10^{-3}$) are obtained, we multiplicate, cell-by-cell, the conductivity by the chargeability to end-up with a normalized chargeability tomogram (expressed in S m^{-1}).

2025) and the data from Casotti *et al.* (2025a, b) for carbonates. Here again the same trend is observed. Fig. 5 demonstrates that, for both sedimentary and volcanic rocks, surface conductivity is controlled by the ratio between the CEC and the tortuosity (defined as the product of the formation factor by the porosity). Figs 3–5 validate the dynamic Stern layer model for both sedimentary and volcanic rocks showing outcrops at the test site (Fig. 2). The DSL model represents therefore a versatile model that can be used to interpret field measurements.

3 FIELD SURVEY AND ITS INTERPRETATION

3.1. Field survey

Currently, new technological developments have allowed to perform large-scale induced polarization surveys using independent stations for the reception of the injection of the electrical current over AB dipoles (A and B denoting the current electrodes used to inject and retrieve the electrical current in and from the ground, see Fig. 6). The approach we use is a time-domain induced polarization in which an alternating polarity square-wave current is injected in the subsurface (see Martin *et al.* 2020; Bérubé & Bérubé 2022). The use of independent recording stations with independent measurements of the primary and secondary electrical field components completes the acquisition system (Fig. 6). In our case, our induced polarization survey was performed in 2023 through an array of 17 V-Fullwaver recorders (IRIS instruments) recording through two dipoles of M and N electrodes laid out in an L-shape (see the position of the electrodes P1, P2 and P3 in Fig. 6). We also used 17 injection dipoles with three fixed electrodes. The injection data sets are recorded through an I-Fullwaver station to synchronize time-series between the injection and voltage signals. The position of the current and voltage electrodes is shown in Fig. 7. The data density used for the inversion is indicated by the recording points plotted on the digital elevation model in Fig. 8 (see also Glaser *et al.* 2021, for such a way to plot the data). The resulting data distribution shown in Fig. 8 is used to ensure a good sensitivity over the entire area of interest.

The source signal is produced by a VIP-5000 squared signal injector and injection current values range from 1 to 4 A, with stacking of 1 s on-off signals ranging from 100 to 300 measurements (see Fig. 9 for an example and Fig. 10 for selected decay curves for different ABMN quadrupoles). The automatic stacking was performed arithmetically to achieve a good signal-to-noise ratio for the measurements. The maximum distance between two electrodes in the same survey was 1.5 km and the maximum pseudo-depth reached is ∼545 m (see Figs 7 and 8). The topography and coordinates of each electrode have been recorded with a Garmin Etrex 30 GPS (Global Positioning System) with a precision of 2 m. The filtering process is performed through two steps: (i) the automatic removal of voltage decays with abnormal shapes with respect to an exponential-like decay (this is done by looking at the semblance between the data and an exponential-type decay) and (ii) the automatic removal of outliers in the two pseudo-sections by running a simple

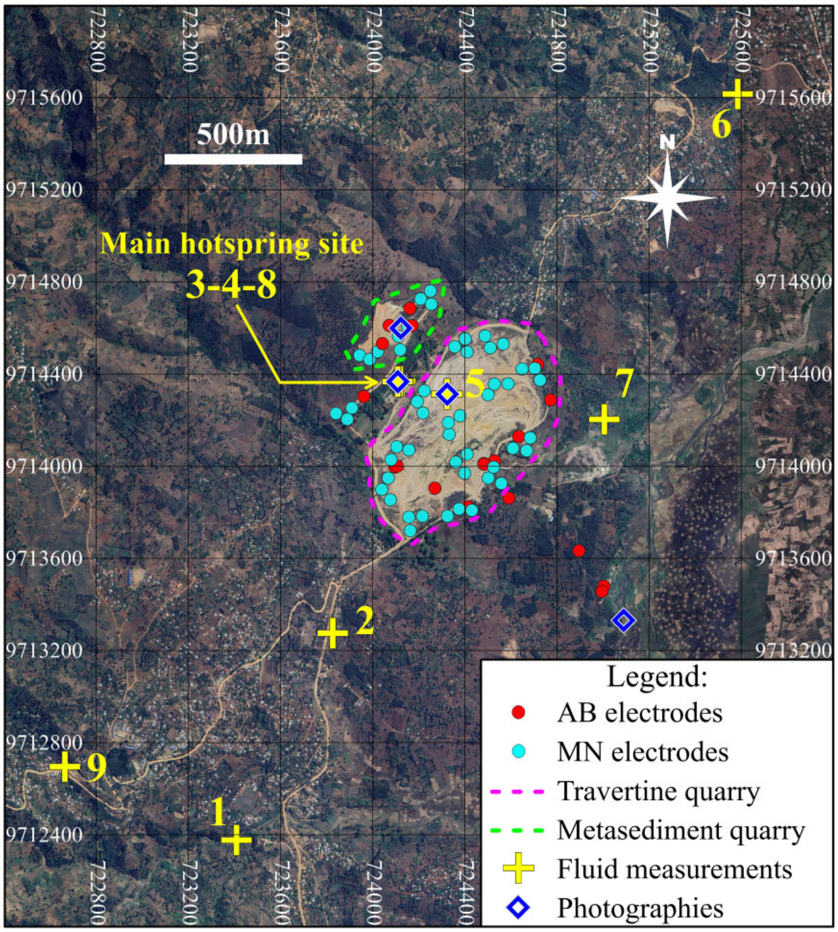

Figure 7. Induced polarization survey with UTM (Universal Transverse Mercator) coordinates showing the position of the current and voltage electrodes and the position of the main hot springs as well as the travertine quarry and metasediments quarry (see Fig. 2). We also indicated the position of the water samples used in Table 1 for the measurements of their conductivity, temperature and pH values, as well as positions of the pictures displayed in Fig. 2.

consistency analysis by looking at the data at each pseudodepth (we use a consistency test by looking at the outliers in the sequence of each pseudodepth with discrepancy higher than three times the standard deviation). This lead to a set of 357 data points of apparent resistivity and chargeability data.

The Digital Elevation Model (DEM) used this study was generated using photogrammetric techniques, based on high-resolution drone imagery and processed with Agisoft Metashape™ software. Image acquisition was carried out by the company Charis UAS employing a DJI Phantom 4 Pro series drone, equipped with an FC6310R camera and differential GPS. The flight mission was designed to cover approximately 0.9 km^2 in and around the active mine site. Data collection was performed over several separate flights, each employing different camera orientations (omega, phi, kappa angles): $-45°$, $0°$, $-180°$ and $0°$, $45°$, $-90°$, to optimize image overlap and improve 3-D reconstruction quality. The average flight altitude during image capture was maintained at 9.24 m above ground level.

Agisoft Metashape was selected as the primary processing software. The drone imagery was pre-processed and processed in Metashape following the conventional photogrammetric workflow, including photo alignment (to generate a sparse point cloud), optimization of camera alignment, dense point cloud generation, mesh construction and DEM creation. Following each iteration, camera alignment was re-optimized to refine positions and orientations. The completed DEM offers a detailed and accurate representation of the mine site's topography, with a spatial resolution of 5.1 cm per pixel.

In situ measurements of surface water characteristics have been conducted on both cold and hot springs, streams and rivers, using a multiparameter probe (pH—precision 0.01, conductivity—precision 0.6 per cent, temperature $\pm$ 0.1 °C) from Horiba (model Laqua 200). The probe was calibrated every day before field activities with solutions of known conductivities. Sites of measurements (labelled 1 to 9 in Table 1) were chosen with the objective of characterizing every type of accessible surface waters encountered at the test site. The conductivity and temperature measurements are provided in Table 1. The relatively low amount of rain precipitation during the field mission implies that streams and rivers were not composed of pure run-off, but probably a mix between base flow issued from resurgences upstream and run-off. Samples from each lithology were also recovered from the site and their connected porosity were measured through Archimedes principle, with results displayed in Table 2. The porosity of metasediments is in the range 8–15 per cent, 22 to 34 per cent for travertine, and 7 to 25 per cent for basalt.

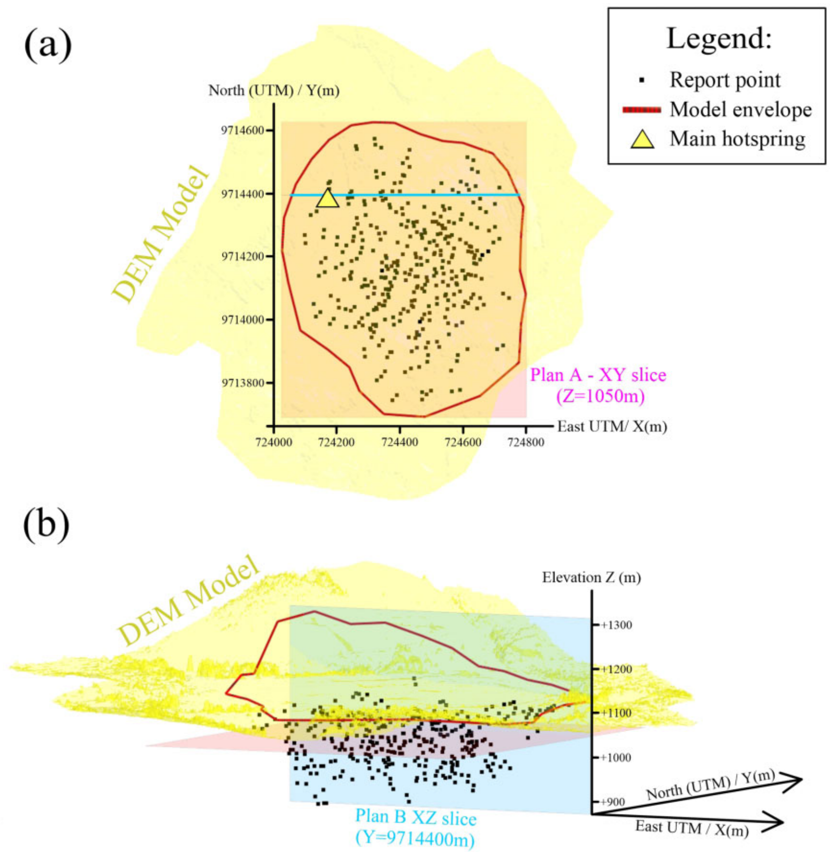

Figure 8. 3-D representation of the survey. (**a**) Top view of the report points and model envelope and main hotspring location. (**b**) South–East view. Plane A and Plane B of interpretation are here displayed, and the ground surface is represented with the use of the Digital Elevation Map (DEM).

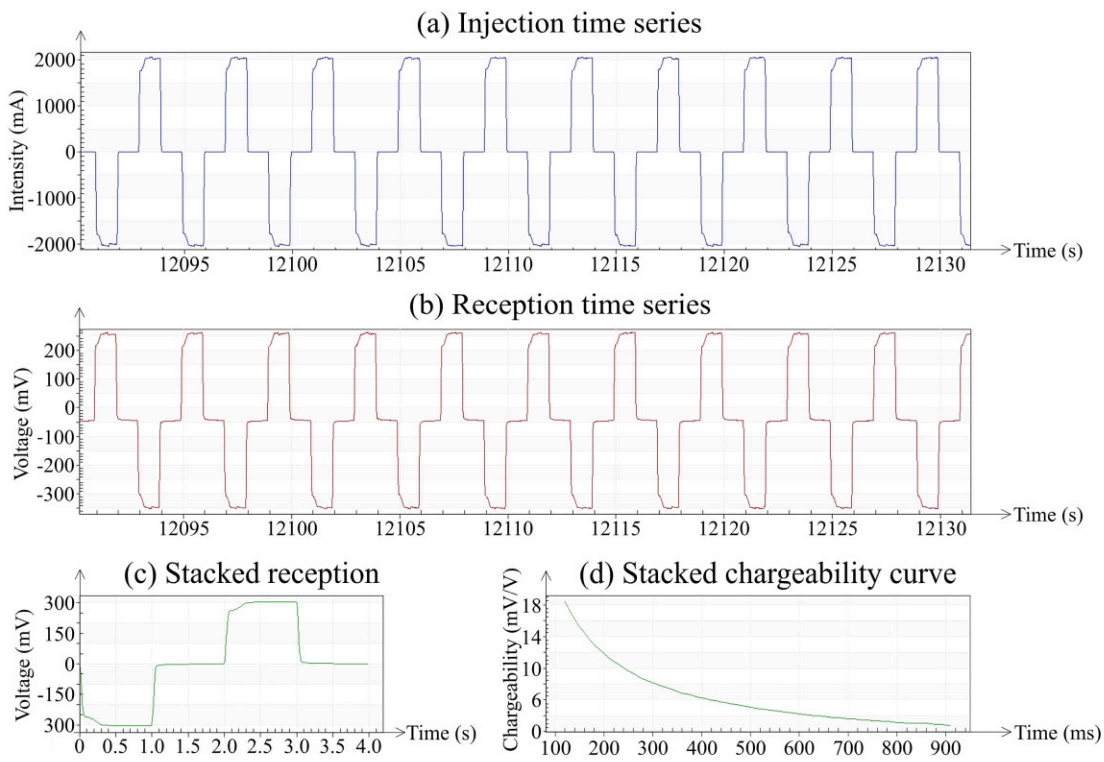

Figure 9. Raw data time series and stacking. (**a**) Current injection time-series for a dipole AB. (**b**) Corresponding voltage time-series for a dipole MN at one recording station. (**c**) Stacked voltage curve. (**d**) Stacked chargeability decay curve.

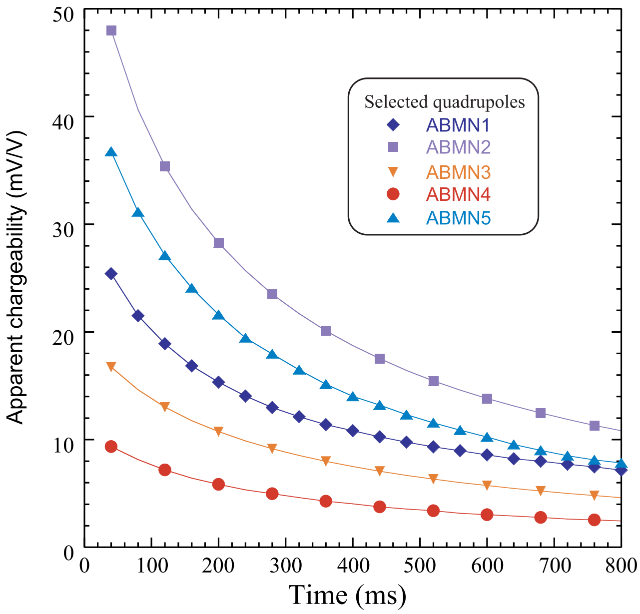

Figure 10. Selected examples of measured decay curves used for the inversion of the chargeabilities. These decay curves display exponential-type decays as usually observed in field surveys. This usually indicates a very good signal-to-noise ratio for the recorded dataset with errors bars roughly inside the size of the symbols. The standard deviations performed on a large number of stacks are the following for the five quadrupoles displayed here: ABMN1 Q = 0.15 mV/V, ABMN2 Q = 0.49 mV/V, ABMN3 Q = 0.05 mV/V, ABMN4 Q = 0.08 mV/V and ABMN5 Q = 0.5 mV/V.

3.2. Tomography

The geophysical data are inverted for the low-frequency resistivity and chargeability with the software Res3Dinv (Loke & Barker 1996) using a 20 × 20 m grid with a four nodes constraint. The algorithm penalizes the roughness of the resulting tomograms (e.g. Weller *et al.* 1996). This high constraint on data inversion and high level of filtering performed helps to reach low RMS (Root Mean Square) errors for deep surveys. The tomography stops at iteration 10 (Gauss–Newton approach, 15 per cent RMS error for the apparent resistivity data). Then, the inversion of the apparent chargeability data yields a 0.68 per cent RMS error.

The inverted models of conductivity and normalized chargeability are shown in Fig. 11 and a cross-plot of the normalized chargeability versus conductivity data is shown in Fig. 12. This type of plot has become a key to comprehend the effect of semiconductors and alteration on the field data including the importance of surface conductivity (e.g. Revil *et al.* 2020, 2021; Piolat *et al.* 2025; Casotti *et al.* (2025a, b). We use an amplification factor of $a = 4.2$ as explained later in the manuscript to correct the time-domain induced polarization data (using an injection time of 1 s) to the normalized chargeability data obtained from frequency-domain induced polarization and defined as the difference between the instantaneous conductivity and the dc—direct current conductivity (see Piolat *et al.* 2025, for a complete analysis of this factor). This figure shows that there are likely two fluids in the system with two different pore water electrical conductivities. Usually, the presence of pyrite or magnetite shows up in the form of vertical trends in the normalized chargeability versus conductivity cross-plot (see fig. 10 of Revil *et al.* 2021). We have also no trace of pyrite or magnetite in the cuttings and core samples from the site. This implies that if we cannot completely rule out the presence of semiconductors, their presence seems to have a minor effect on the overall polarization process, which seems dominated by the electrical double layer at the surface of the mineral grains. For carbonate assuming that the field response is also dominates by surface conductivity, we obtain $R = 0.015$ in close agreement with the value given for pure calcite by Panwar *et al.* (2021). This is consistent with the fact that in the metasediments, the fracture network is filled with carbonates as shown in Fig. 12(a). The metasediment quarry is representative of this invasiveness of carbonate-rich material in the area, as it is exploited for its carbonate content.

The porosity and CEC tomograms are obtained from the conductivity σ-tomograms and normalized chargeability M_n-tomograms using the following relationships.

$$\phi = \left(\frac{\sigma}{\sigma_w} - \frac{M_n}{\sigma_w R}\right)^{1/m}, \tag{5}$$

$$\mathrm{CEC} = \frac{M_n}{\phi^{m-1}\rho_g \lambda}. \tag{6}$$

The porosity obtained in eq. (5) is used in eq. (6) to obtain the CEC. In order to obtain tomograms of the porosity, CEC and temperature, we need some values of the input parameters. First, the values of m, R and λ have been fixed in Section 2. As shown by eq. (6), the CEC is inversely proportional to the chosen value of the grain density. In our analysis, the value of the grain density is taken to be uniform and equal to 2700 kg m^{-3}. For siliciclastic materials, this is usually a good choice in absence of pyrite and magnetite, which may significantly increase the grain density of the material. For carbonates, the grain density of calcite is 2710 kg m^{-3} therefore, we do not expect a high influence of grain density variation over the results provided here. We need therefore to assess the pore water (σ_w) conductivity. The water conductivity has been measured at several locations over the studied area (Fig. 7 and Table 1), including directly at the main hot springs location. As shown, measurements from the local springs range from 0.17 to 0.21 S m^{-1}. To account for the mixing with meteoric water within surface ponds (see Table 1), we hypothesized a dilution factor of around 20 per cent of the hydrothermal fluid with meteoric waters, leading to an assumed $\sigma_w(25\,^\circ\mathrm{C}) = 0.25$ S m^{-1} at depth for the DEEP-ERT-IP model. Furthermore, because of the production of smectite through the alteration process, we can also transform the normalized chargeability values into temperature values as demonstrated in Revil & Gresse (2021), with $M_0 = 5.8 \times 10^{-8}$ S m^{-1}.

$$T = \left(\frac{M_n}{M_0}\right)^{1/2.5} \tag{7}$$

The relationship between normalized chargeability and temperature is related to the degree of alteration at a given temperature, effectively using smectite as a geothermometer (Revil *et al.* 2021). Furthermore the quantities σ, σ_w, M_n and λ have all the same Arrhenius-law (or linear) temperature dependence associated with the effect of temperature on the dynamic viscosity of the pore water and therefore on the ionic mobilities involved in these parameters (see Ghorbani *et al.* 2018; Revil *et al.* 2019 for an extensive discussion). For instance we use $\sigma_w(T) = \sigma_w(T_0)(1 + \alpha_T(T - T_0))$ with $\alpha_T = 0.023/^\circ$C (Revil *et al.* 1998). Some parameters in eqs (5) and (6) (like R, ρ_g and m) are considered to be temperature independent. Eq. (5) allows the cancellation of the exponential (temperature-dependent) terms of the Arrhenius relation when calculating ϕ and CEC. However, since the electrical conductivity

Table 1. Pore water conductivity estimates. The pore water conductivity has been measured at several locations over the studied area. It has been measured directly at the main hot spring location (see position in Fig. 1). The measurements from the local springs range from 0.172 to 0.21 S m^{-1}. UTM: Universal Transverse Mercator, masl: meters above sea level.

Label	X UTM	Y UTM	Z masl	Water type	σ_w (S m^{-1})	pH	T (°C)
1	723 409	9712 377	1103	River	0.0130	8.2	23.5
2	723 827	9713 275	1133	Water pond	0.0116	5.8	25.0
3	724 120	9714 369	1168	Hydrothermal pond	0.1796	6.5	35.0
4	724 110	9714 368	1171	Hydrothermal pond	0.1960	6.3	47.0
5	724 323	9714 313	1165	Hot spring resurgence	0.2000	6.4	51.7
6	725 585	9715 615	1146	River	0.0165	8.0	27.2
7	725 006	9714 203	1090	Spring	0.1720	8.3	26.4
8	724 109	9714 367	1171	Hot spring	0.2100	6.4	48.0
9	722 664	9712 696	1255	Spring	0.0066	6.2	24.0

Table 2. Connected porosity measurements on rock samples through Archimedes methodology. For Travertine 3, the weighing obtained in unsaturated condition underestimate the connected porosity because of water leakage.

Label	Connected porosity
Altered Metasediment	0.150
Low alteration Metasediment	0.075
Travertine 1	0.227
Travertine 2	0.295
Travertine 3	0.340
Altered basalt	0.250
Low alteration basalt	0.071
Low alteration basalt	0.065

tomogram is based on observed field signals and therefore inherently reflects *in situ* temperature conditions, we need the temperature tomogram to correct for the temperature field. Therefore in eqs (5) and (6), the measured σ-field and pore water conductivity are corrected from the temperature field obtained with the normalized chargeability distribution. This process plays an essential role in the determination of the subsequent CEC and porosity distributions.

Finally, as shown in several research works in induced polarization (e.g. Piolat *et al.* 2025 and references therein), we apply for the CEC tomograms a factor of amplification on M_n determined from the characteristics of the time-domain induced polarization data acquisition parameters (current injection time, dead time and duration of the time-windows measuring the decay of the secondary field). The reason is that the normalized chargeability measured by injecting a source current with a period of 1 s is necessarily smaller than the normalized chargeability determined in the frequency-domain as the difference between the instantaneous conductivity and the dc—direct current conductivity. Data analysis supported by knowledge of prior laboratory measurements indicates an amplification factor given by $a = 4.5$. The result is shown in Fig. 13.

4 INTERPRETATION OF THE FIELD RESULTS

On a geomorphological point of view, the site of investigation marks the transition between a mountainous system, and the flat alluvial valley. The metasediments constitute this sharp relief upwards, while basalts constitute the hills surrounding the travertine quarry, as well as the basement of the alluvial valley downwards (Fig. 2). Those three entities are thought to have three distinct hydrogeological behaviours. Fractured metasediments, with high slope and thin regolith, are prone to high run-off and low recharge of aquifers. However, this recharge is essential for the deeper hydrothermal system. Basalts are capped with a thick lateritic regolith (10 m and more), hosting a superficial aquifer. Alluvial deposits also host an aquifer, related to the river.

The hot spring of Mashyuza results from deep, rift-related, fracturing of the metasedimentary basement. Reaching the surface, the warm waters are spread through recent fractures cross-cutting the travertines. This epikarstic system has been reactivated by the exploitation of the quarry, as recent sinkholes and eroded conduits can be observed in the field.

The fluid measured at the main hotspring and hotspring resurgence in the central part of the quarry is composed of carbonate-rich water and gas (99 per cent CO_2), depositing the travertine and carbonate mud in excess of 50 m thickness. Conductivity, pH and temperature measurements tend to show that there are interactions between run-off, shallow aquifers and deep warm waters. Measurement N°7 in Table 1, from a cold spring located downstream from the travertine quarry, is representative of this mixing, with conductivity comparable to the hydrothermal ones, and low temperature, suggesting interference between the hydrothermal flow and the shallower cold aquifers.

The mixing is thought to occur during the travel of the warm water from its main point of emission close to the border fault located at the upper limit of the travertines, through the travertines and mostly at the edges of the travertine deposits where they are interdigited with the laterites overlying the basalts. The permeability of the travertines is very high in the epikarst and the most recent fractures, between the beds of travertines, as well as in an evolving facies that can be observed at different levels in the quarry, incorporating vegetal debris. Those different types of permeability are favourable to the interactions between warm and cold peripheric waters.

Two sections of interpretation are here provided from the 3-D geophysical model information. Section A in the *XY* plane at an elevation $Z = 1050$ masl (Fig. 14), and section B in the *ZX* directions, at $Y = 9714\,400$ m UTM (Fig. 15). Section A shows the extension of the hydrothermal activity over the studied area, within a corridor bounded by two main structures, each of which is composed of the interaction between two main structural trends (N170 and N70). Structure α is controlling the contact between the basement and infilling basalts and travertines on the west and structure β is controlling the extension of the hydrothermal activity on the east. This corridor could be the trace of the damage zone of a main fault, with the fault core along the α-structure as described in other faulted basement contexts (Walter *et al*. 2019, Bertrand *et al.* 2021).The structural and kinematic data set confirms our geophysical

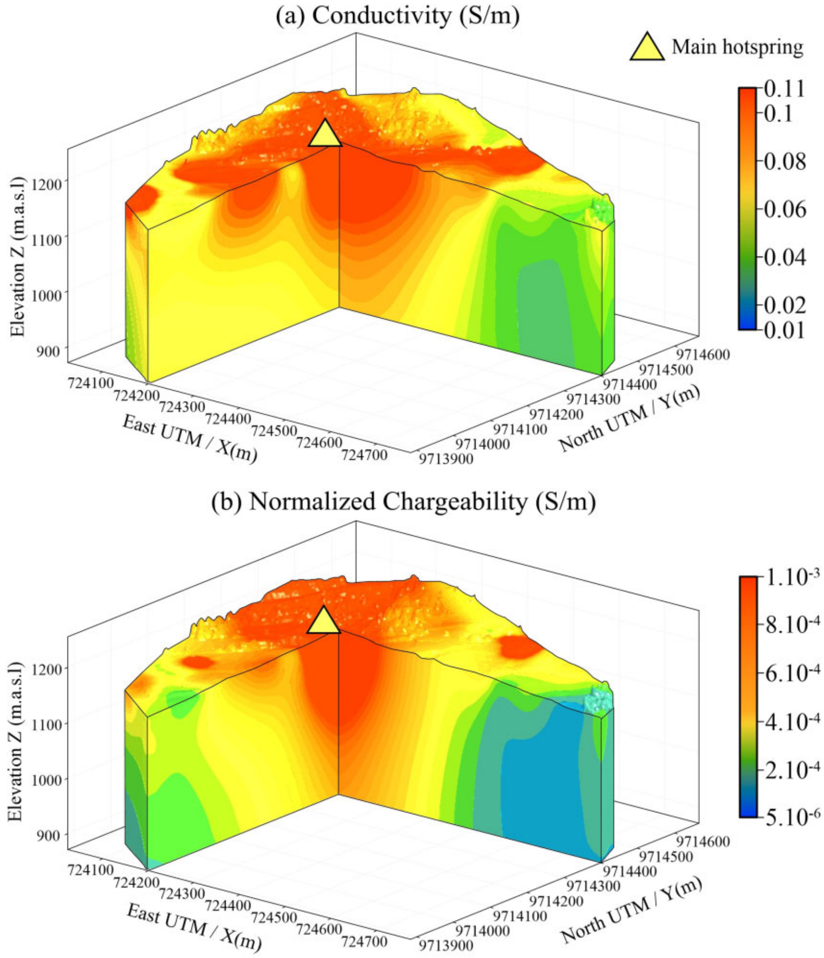

Figure 11. Induced polarization tomograms. (**a**) Electrical conductivity tomogram showing a distribution covering 2 orders of magnitude. (**b**) Normalized chargeability tomogram showing a distribution covering 2.5 orders of magnitude. We can observe a plume characterized by high values of the conductivity ($\sim$0.1 S m^{-1}) and normalized chargeability ($\sim$1 $\times$ 10^{-3} S m^{-1}) associated with hydrothermal alteration visible around the main hotspring location, which position is materialized by the open triangle.

interpretation in terms of azimuth dipping and tectonic system, with the main hydrothermal horizon dipping east within a normal extension system (Fig. 16). The hotspot associated with the main hotspring lies along structure α at the interaction of the two structural trends. We observe here that the concentration of hydrothermal alteration indicated by the assessment of surface conductivity does not align with overall porosity distribution. The maxima of modeled porosity are located at the middle of the extensional area while maxima of assessed temperature and CEC concentrate in the vicinity of the hot spring itself. In terms of values, the temperature model assessment is consistent with the fluid temperatures made at the ground surface. The maximum temperature is 51 °C in the resurgence within the travertine quarry *versus* 49 °C at the same location for the geophysically derived model. The temperature is measured to be 65 °C at a depth of 150 m within the hotspot through a previous well set up in the metasediment quarry. At the same location, the temperature derived from the geophysical data is 61 °C.

The CEC values obtained through the tomography are also consistent with the presence of carbonates. For carbonates the typical range is between 1 meq/100 g (Revil *et al.* 2020) to 9 meq/100 g (see Panwar *et al.* 2021) depending on their clay content. For altered silicate rock, the CEC is typically above 10 meq/100 g (Revil *et al.* 2021). Regarding the porosity, we obtain a range of values in between 0.25 to 0.50, therefore quite high. The upper value is consistent with the porosity of travertine obtained at other sites. For instance, Revil *et al.* (2020) obtained a porosity value of 0.51 for travertine at a landslide site in France. Table 2 provides porosity values close to 0.30 and also consistent with the porosity tomogram. The basalts have a substantially smaller porosity, around 0.07, while the sediments have intermediate values. To date, there are no data on the mineralogical composition of the hydrothermalized zones. Travertine-rich areas generally overlie fault zones in which hydrothermal fluids circulate (Hancock *et al.* 1999; Brogi *et al.* 2021). Knowing the initial compositions of the metamorphic rocks and volcanic rocks beneath the travertines on the one hand, and the temperature field on the other, potential hydrothermal paragenesis can be assessed by following the synthesis proposed by Battaglia *et al.* (2004) and Pereira *et al.* (2024), respectively, for protolith on two edges. Thus, the attended paragenesis are, Illite + Chorite + interstatified Illite-Smectite for the metamorphic rocks and Kaolinite + Smectite ± opale ± cristobalite ± Pyrite for the tholeiitic rocks.

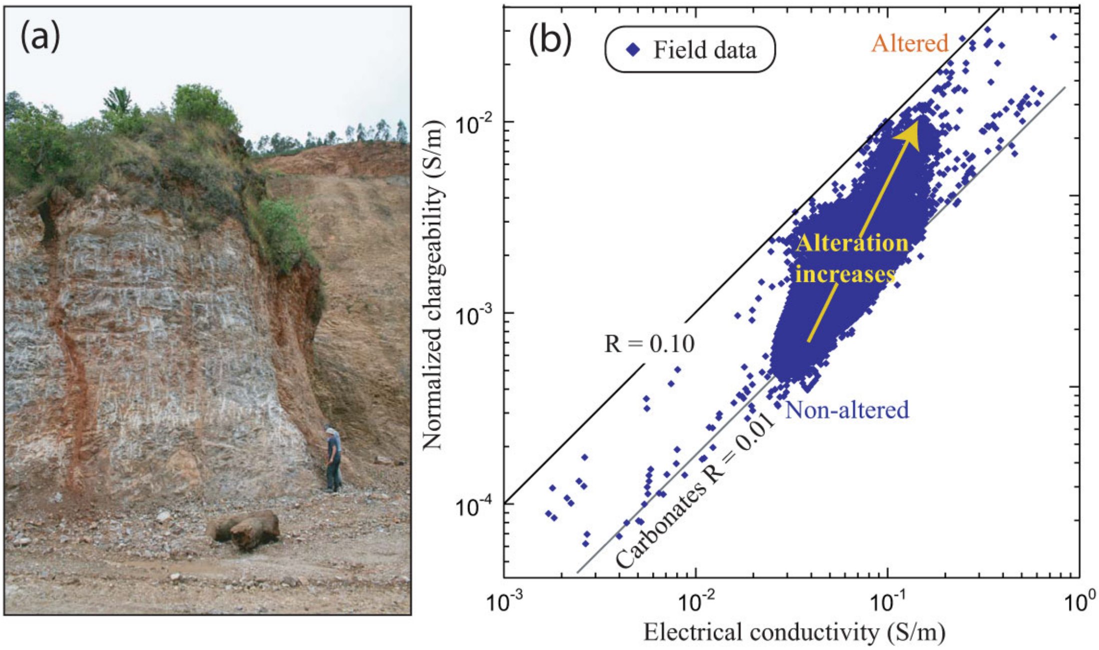

Figure 12. Analysis of the cross plot between normalized chargeability and electrical conductivity. (**a**) Picture showing how the cracks and faults are partially filled with carbonates at the test site. (**b**) Normalized chargeability versus conductivity plot showing the position of the field-gathered data points. The data set seems to display the existence of two lithologies at the test site. The volcanic rocks and sediments and metasediments have a conductivity dominated by surface conductivity being close to $R = 0.10$. The carbonates have a value for R slightly above the value 0.01 corresponding to pure calcite (see Panwar *et al.* 2021).

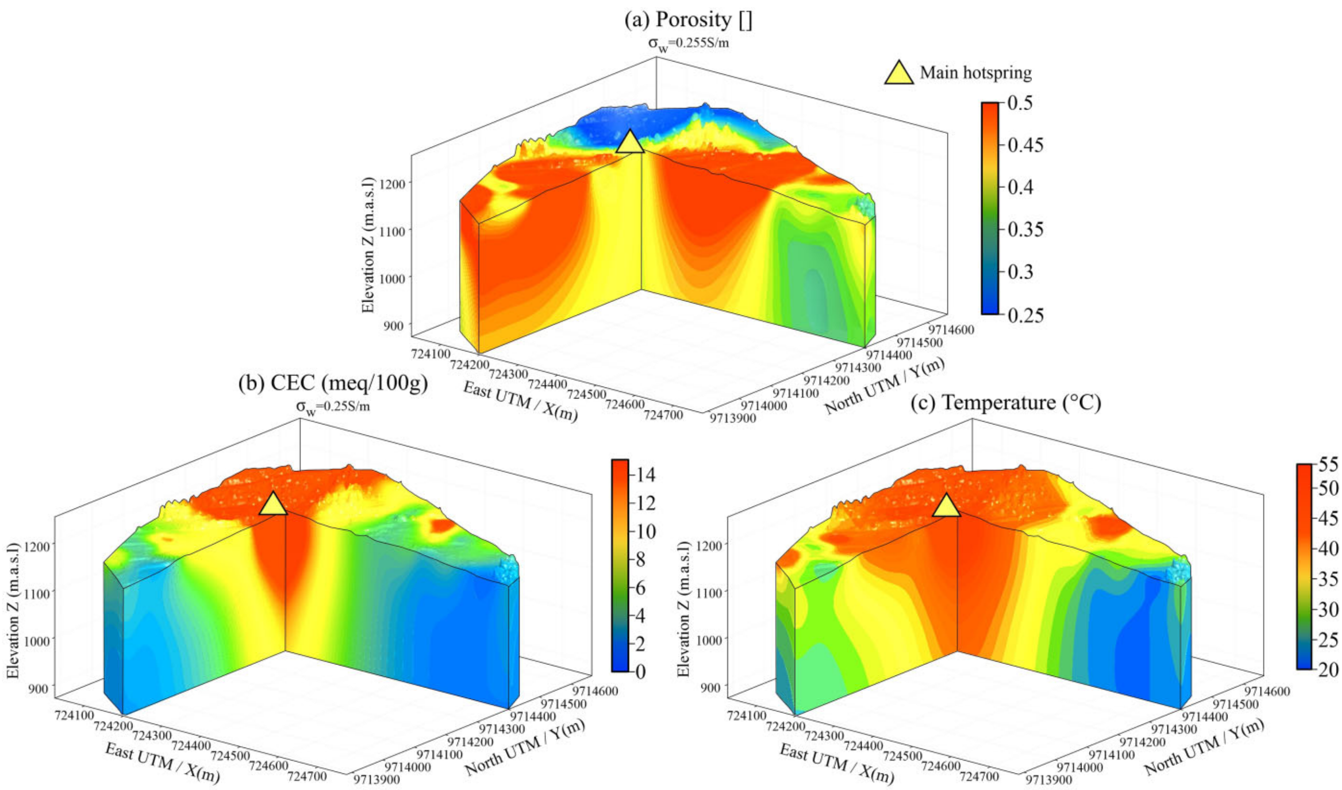

Figure 13. Application of the petrophysical model to the field data shown in Fig. 6. (**a**) Porosity tomogram (unitless, fraction). (**b**) Cation Exchange Capacity (CEC) tomogram (expressed in meq/100 g with 1 meq/100 g $= 963.20$ C kg^{-1}). (**c**) Temperature tomogram (expressed in °C). The temperature of the hot spring (materialized by the triangle) is close to 52 °C consistent with the tomogram.

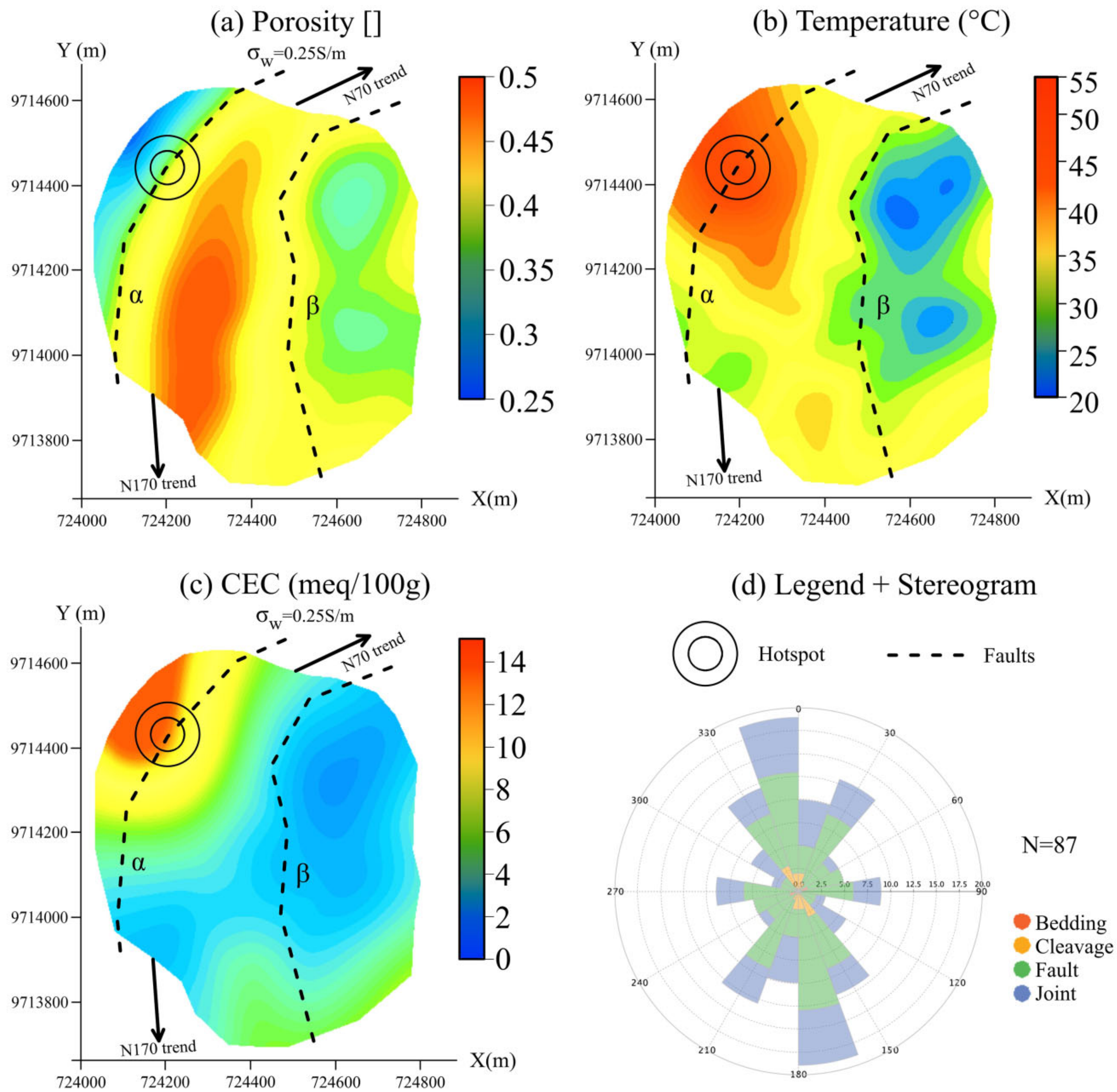

Figure 14. Properties along Plane A ($Z = 1050$ masl, meters above sea level) with structural interpretation. (**a**) Porosity horizontal cross-section. (**b**) Temperature horizontal cross-section. (**c**) CEC horizontal cross-section. (**d**) Field Rose Plot showing the orientation of the main structural features.

Looking at the East–West slice crossing the hotspot described earlier (Fig. 15), we observe the dip-parallel architecture of this local extensional basin. The two structures α and β accommodate the major porosity signal. The West border displays metasedimentary formations, with the lowest model porosities, in contact with infilling rift formations: travertines laying over volcanic formations, which have a high porosity east of the α-structure and whose porosity decreases west to this structure.

The main issue with the model is its consideration of a unique pore fluid, at 0.25 S m^{-1} (25 °C) within the entire 3-D model. This value is within the range of independent geochemical analysis performed by Sunguti *et al.* 2024 on site, with a variation for hot-spring fluid conductivity in between 0.256 and 0.293 S m^{-1}. Meanwhile, it is likely that this hydrothermal fluid percolates upwards and mixes with surface water. This mixing supports the temperature tomogram and the observed decrease in salinity away from the rising plume. As observed in the conductivity tomogram, and from the hypothesis of a relatively constant stratigraphy going westwards, we suspect the variation of conductivity not to be caused only by porosity variations, but also by mixing of the hydrothermal fluid and/or decrease in ionic content through mineral precipitation. This could explain the evolution of calculated porosity between the two interpreted structures and materialized by the hydrothermal flow arrows, and the decrease in measured fluid conductivity from the main hot spring values (≈ 0.2 S m^{-1}, 25 °C) to the outside quarry measurement (measurement n°7 at 0.17 S m^{-1}, 25 °C). As expected, lower fluid conductivity are observed from the water sampling in the eastwards direction. At the same time, higher porosities than

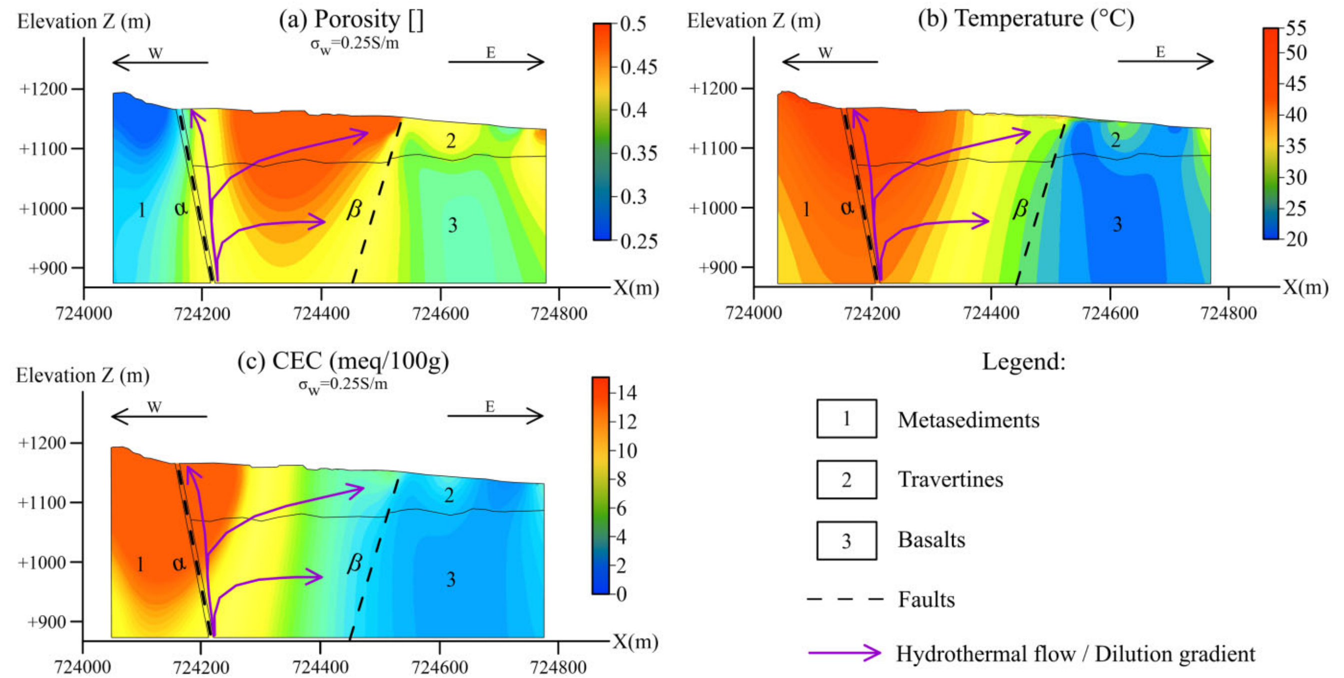

Figure 15. Physical properties along Plane B ($Y = 9714\,400$ m). (**a**) Porosity vertical cross-section. (**b**) Temperature vertical cross-section. (**c**) CEC vertical cross-section. We also indicated the geological units as well as the main flow paths and structural interpretations.

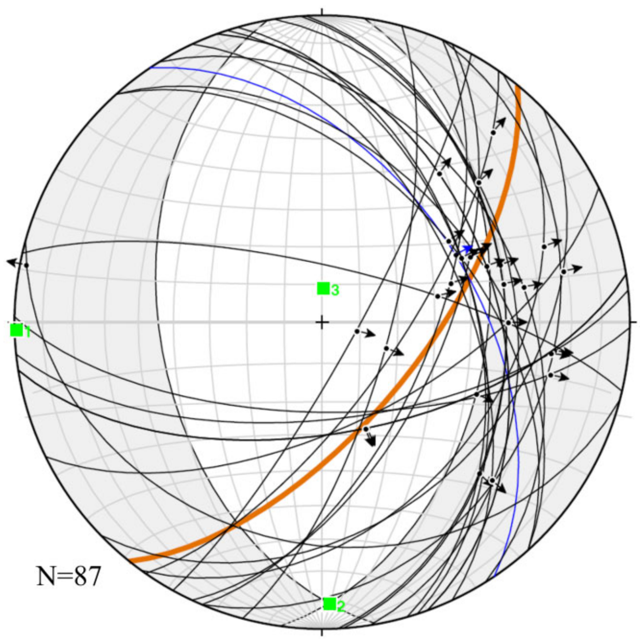

Figure 16. Fault-kinematic measurements within basement fault zone in traprock quarry above Amashyuza hot springs. 29 fault-striation pairs. Thick orange plane approximates upper surface of outcropping fault zone determined from virtual outcrop model, with strike 039 N, dip 64° SE. Kinematic indicators (arrows showing movement of hanging wall) indicate sinistral oblique normal slip on the fault. An unweighted moment tensor solution is indicated by 'beachball' quadrants, with principal axes as numbered green squares, consistent with nearly horizontal E–W extension.

estimated are observed in the same direction if we assume a stratigraphical continuity. We can switch our modelling process from fixing the fluid conductivity in the model to fixing the porosity to solve the linear system of equations.

For assessment of this dilution process within the conductivity anomaly, we then opted for a demonstrative qualitative analysis of the travertine block with fixed setting of the porosity while making the fluid conductivity as a variable (Fig. 17). We extracted a slice of the 3-D model corresponding to the travertine body interpreted in Fig. 15, with a setting of the porosity at 45 per cent for the travertines, the mean value of porosity within this model block. The fluid conductivity curve shows a potential indicator of this dilution and/or degassing process, as we observe a steady increase of salinity between α-structure at X(α)=724 180 m and β-structure at X(β)=724 750 m, which could be explained by degassing and loss of -0.67 g L^{-1} of Ca^{2+} (-1.04 g L^{-1} of carbonic acid) between the maximum and minimum fluid conductivities. In absence of travertine precipitation and degassing but considering dilution to explain the fluid conductivity distribution, we need a dilution from the structures α and β to be roughly estimated 50 $\pm$ 10 per cent.

There is of course still an uncertainty within the characterization due to the duality of choosing a constraint on porosity or fluid conductivity, as for the used equation system there is still a variable the geophysicist need to fix within the model (which could be done uniformly or by a gradient hypothesis). In travertine hydrothermal systems, the very high permeability and porosity created through induced dissolution, macrofractures and karst formation processes, are of great variability. The high porosities calculated from the fixed fluid conductivity at 0.25 S m^{-1} could be explained by such processes. Moreover, our porosity measurements in Table 2 tend to lead us to a very high porosity system, because only coherent samples

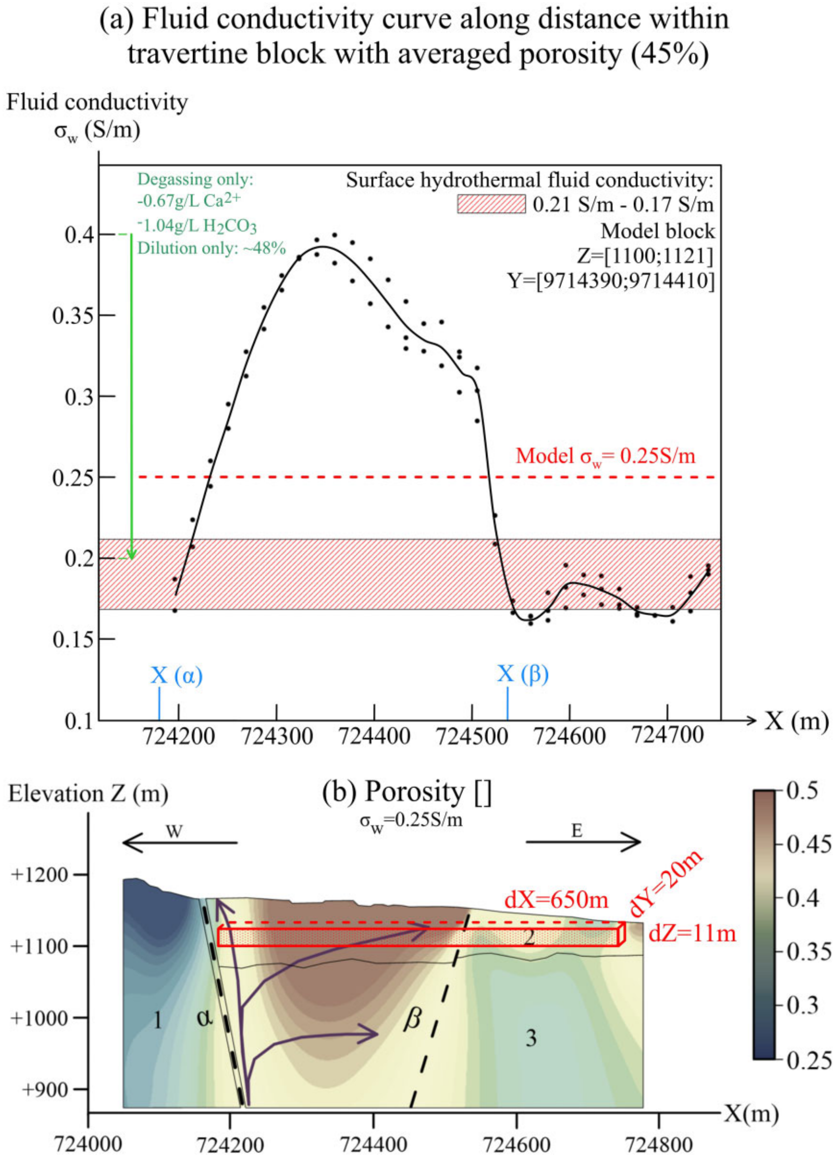

Figure 17. Ground water mixing assessment in the hypothesis of a fixed porosity block. (**a**) Fluid conductivity curve within the described extracted travertine block and fixed porosity hypothesis (45 per cent) and examples of possible explanations in fluid conductivity variations in terms of dilution or degassing of CO_2. (**b**) Display of the concerned block of travertines from the porosity Plane B view of Fig. 15. E and W are East and West directions. α and β denote the main faults discussed in the main text. The numbers 1, 2 and 3 label the three compartments discussed in the main text.

were able to be transported for analysis, giving us a first underestimation of the system larger scale porosity, and second because of the underestimation of porosity for travertine sample n°3 due to leakage through the observed tubular macroporosity (centimetric) for wet mass measurements. On the other hand, and while probably not reaching such extremes, fixing the fluid conductivity at 0.4 S m^{-1} (25 °C) at the maximum of the fluid conductivity curve in Fig. 17 in the hypothesis of a dilution of hydrothermal surface waters could also be a significant factor of our modeled porosities. Such value for the fluid conductivity would not affect porosity tomogram geometries but would shift linearly the displayed results (and associated colour display) from [0.25;0.5] (unitless) to [0.19;0.39] (unitless). Some ways to solve this would be to use other geophysical/petrophysical methodologies (such as spontaneous potential or microgravimetrics for geophysical methods or spectral sample polarization for petrophysical methods). This would be done with the aim of setting a porosity or fluid conductivity gradient within the model, to solve the fluid conductivity petrophysical system as a determined inverse problem, and to link the geophysical hectometric scale to the sample laboratory scale.

We observe that within conductive reservoirs, induced polarization surveying can struggle to establish the delineation of lithologies due to the effects of saline fluid gradients and surface conductivity localizations (see Piolat *et al.* 2023 for similar conclusions). Drilling for the geothermal resource here greatly benefits from temperature and porosity modelling, as it helps to characterize the flow uprising and lateral path of the hydrothermal fluid, from its source to its percolating reservoir, leading to better detection of temperature and salinity fields for geothermal unit design. We observe that the temperature results are consistent with fluid sampling and that the

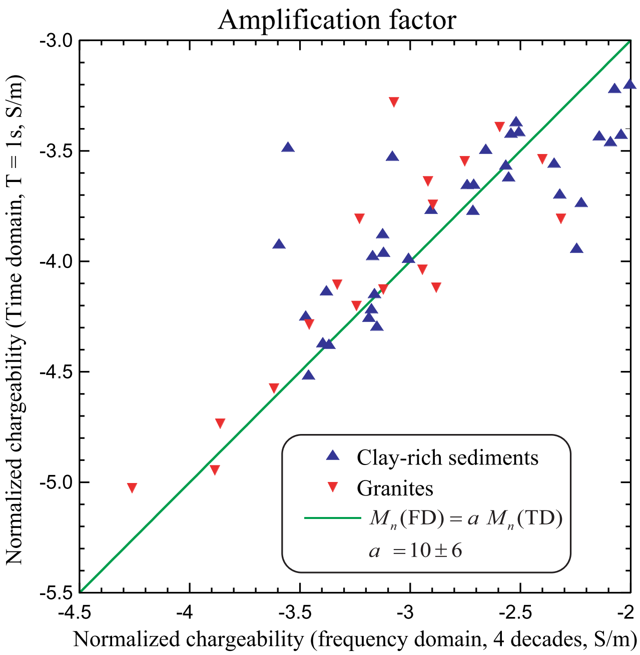

Figure 18. Amplification factor between the normalized chargeability determined in the time domain (current injection with a period $T = 1$ s, a dead time of 100 ms, and an integration time of 0.1 s) and the normalized chargeability determined in the frequency domain (4 to 5 decades in the dispersion of the in-phase conductivity outside the frequency-range dominated by the Maxwell–Wagner polarization).

discrimination between conductivity processes helps geophysicists and related geoscientists to go deeper in the analysis of structural controls, alteration intensity, and reservoir properties and geometries.

5 DISCUSSION

We want to provide below additional insights regarding the applicability of our model to other geothermal sites in order to better contextualize the application and limitations of the DSL model at geothermal sites. The questions we want to tackle are the following: Can the DSL model and induced polarization be used in characterizing high-temperature geothermal systems? What if the geothermal system has high volumes of semiconductors? Can the DSL model and induced polarization be used for high salinity systems? And finally how to calibrate the amplification factor to correct the normalized chargeability in field-time-domain induced polarization to bring back the values to the normalized chargeability determined in the laboratory using frequency-domain induced polarization?

Our model can handle different lithologies and alteration schemes, salinity variations and presence of semi-conductors and therefore can be used to forward-modelling the induced polarization response in complex geothermal systems when coupled to multiphase reactive transport modelling codes. That said, induced polarization has strong limitations. In the case of high salinity fluids, the ratio between polarization parameters (normalized chargeability or quadrature conductivity) and the conductivity parameters is very small (small chargeability and phase values). In this situation, induced polarization can become hard to measure. Our approach requires maximizing both the injected current and stacking. In the case of the presence of high volume fraction of semiconductors (pyrite, magnetite), the induced polarization response may become hard to decipher between non-metallic and metallic components of induced polarization. The normalized chargeability-versus conductivity plot is the key of the analysis in conjunction with any additional data that can be used (lithology and temperature information from boreholes, petrophysical measurements in the laboratory of some representative rock samples). Furthermore, the geophysical geothermometer used here only works for a relationship between CEC and alteration controlled by the presence of smectite, which disappears above 220 °C. Consequently, temperature cannot be imaged above this critical temperature (see Revil *et al.* 2021). That said, induced polarization can be used to provide useful constraints on scenarii of thermal modelling using all the prior information that can be merged. It also complements other geophysical data including seismic, gravity and magnetic data and can be used in some joint inversion modelling.

The next point we want to discuss is the amplification factor for the normalized chargeability a. Its value depends on the characteristics of the spectra. We can obtain it in the laboratory by comparing the normalized chargeability obtained in the frequency-domain (looking for instance at the dispersion of the in-phase conductivity between two frequencies) with the data obtained in the time-domain using a given period of current injection, dead time and integration time for the secondary voltage. The data reported in Fig. 18 indicates that a range from 4 to 16 with an average around 10. In the present paper, we know from our previous studies in this serie that surface conductivity dominates the conductivity response in low-salinity environments. By having the normalized chargeability/conductivity trend close to the slope given by $R = 0.10$ in Fig. 12b, we obtained a reasonable value of $a = 4.2$. Clearly additional work is needed to further refine the value of a.

6 CONCLUSIONS

The DSL model with its ability to discriminate and evaluate conductivity processes provide geophysicist a great tool for tracking and imaging geothermal targets. The development of distributed acquisition systems in DEEP-ERT-IP enables the modelling of porosities, temperature fields, and CEC values within the investigated volumes. Through this methodology and with the input of fluid conductivity measurements, geophysicists can detect structural controls and hotspots within overall conductive anomalies. We applied this methodology on the hydrothermal travertines of Mashyuza with great concordance between the temperature modelled through geophysics and temperature measured from fluid measurements. Alteration and porosity assessment are also coherent with geological knowledge of this hydrothermal target, and porosity deviations can actually detect fluid migration and dilution processes within the geoelectrical models.

ACKNOWLEDGMENTS

We thank the Région Grand-Est and CNRS (Centre National de la recherche Scientifique) for funding the PhD thesis of Loris Piolat, Lithium de France and ADEME (Agence De l'Environnement et de la Maîtrise de l'Energie) for funding the PhD thesis of Pierre Cosme, the EDCL for their warm welcome, logistical support and technical supports. This a contribution of the WP11 'Geothermal Village' of the LEAP-RE programme that financing and enabling this research work. We thank the Editor, Tina Martin and two anonymous referees for their very constructive and useful comments and their valuable time in reviewing our work.

DATA AVAILABILILY

The data used in this manuscript are available upon request to the corresponding author.

REFERENCES

Aran, D., Maul, A. & Masfaraud, J., 2008. A spectrophotometric measurement of soil cation exchange capacity based on cobalthexamine chloride absorbance, *C. R. Geosci.,* **340**(12), 865–871.

Archie, G.E., 1942. The electrical resistivity log as an aid in determining some reservoir characteristics, *Trans. AIME,* **146,** 54–62.

Battaglia, S., Leoni, L. & Sartori, F., 2004. The Kübler index in late diagenetic to low-grade metamorphic pelites: a critical comparison of data from 10 Å and 5 Å peaks, *Clays Clay Miner.,* **52,** 85–105.

Bernard, M.-L., Zamora, M., Géraud, Y. & Boudon, G., 2007. Transport properties of pyroclastic rocks from Montagne Pelée volcano (Martinique, Lesser Antilles), *J. geophys. Res.,* **112,** B5, doi:10.1029/2006JB004385.

Bertrand, L., Géraud, Y. & Diraison, M., 2021. Petrophysical properties in faulted basement rocks: insights from outcropping analogues on the Western Rift shoulders, *Geothermics,* **95,** 102 144, doi:10.1016/j.geothermics.2021.102144.

Bérubé, C.L. & Bérubé, P., 2022. Data-driven modelling of time-domain induced polarization, *Geophysics,* **87**(3), E135–E146.

Börner, F.D. & Schön, J.H., 1991. A relation between the quadrature component of electrical conductivity and the specific surface area of sedimentary rocks, *The Log Analyst,* **32,** 612–613.

Brogi, A., Capezzuoli, E., Karabacak, V., Alçiçek, M. & Luo, L., 2021. Fissure ridges: a reappraisal of faulting and travertine deposition (travitonics), *Geosciences,* **11,** 278, doi:10.3390/geosciences110 70278.

Bücker, M., Flores Orozco, A., Undorf, S. & Kemna, A., 2019. On the role of Stern-and diffuse- layer polarization mechanisms in porous media, *J. Geophys. Res. Solid Earth,* **124,** 6, 5656–5677.

Casotti, C., *et al.* 2025a. Induced polarization applied to landslides. Part 1: imaging hydraulic barriers, *Geophys. J. Int.,* **242,** 1–26.

Casotti, C., *et al.*, 2025b. Induced polarization applied to landslides. Part 2: anatomy and water content tomography of a mudflow, *Geophys. J. Int.,* **242,** 1–25.

Cerepi, A., 2004. Geological control of electrical behaviour and prediction key of transport properties in sedimentary porous systems, *Colloids and Surfaces A: Physicochem. Eng. Aspects,* **241,** 281–298.

Chorowicz, J., 2005, The East African rift system, *J. Afr. Earth Sci.,* **43**(1), 379–410.

Dias, C.A., 1972. Analytical model for a polarizable medium at radio and lower frequencies, *J. geophys. Res.,* **77,** 4945–4956.

Dukhin, S.S. & Shilov, V.N., 1974. *Dielectric Phenomena and the Double Layer in Disperse Systems and Polyelectrolytes*. Wiley, New York.

Ebinger, J.C., 1989. Geometric and kinematic development of border faults and accommodation zones, Kivu–Rusizi Rift, Africa, *Tectonics,* **8**(1), 117–133.

El Alam, J., Revil, A. & Dick, P., 2025. Induced polarization of clay-rich materials. 4. Water content and temperature effects in bentonite, *Geophysics,* **90**(2), MR39–MR54.

El Alam, J., Revil, A. & Dick, P., 2024. Induced polarization of clay-rich materials. 5. Influence of hyperalkalinity in bentonite, *Geophysics,* **89**(6), E267–E279.

Ergen, T. & Suckert, L., 2021. "Crises" as catalysts for more sustainable futures? The case of the first oil crisis and the role of multilayered interpretative struggle, *Max Planck Institute for the Study of Societies: Cologne,* **22**(2), 15–23. https://econsoc.mpifg.de/43430/04_Ergen_Suckert-NL_22-2_March2021.pdf.

Finizola, A. *et al.* 2006. Hydrogeological insights at Stromboli volcano (Italy) from geoelectrical, temperature, and CO_2 soil degassing investigations, *Geophys. Res. Lett.,* **33,** L17304, doi:10.1029/2006GL026842.

Fixman, M., 1980. Charged macromolecules in external fields. I. The sphere, *J. Chem. Phys.,* **72,** 5177–5186.

Flores Orozco, A., Gallist, J., Steiner, M., Brandstätter, C. & Fellner, J., 2020. Mapping biogeochemically active zones in landfills with induced polarization imaging: the Heferlbach landfill, *Waste Manag.,* **107,** 121–132.

Flores Orozco, A., Williams, K.H., Long, P.E., Hubbard, S.S. & Kemna, A., 2011. Using complex resistivity imaging to infer biogeochemical processes associated with bioremediation of an uranium-contaminated aquifer, *J. geophys. Res. Biogeosciences,* **116**(G3), G03001, doi:10.1029/2010jg001591.

Flóvenz, O.G., Spangenberg, E., Kulenkampf, J., Arnason, K., Karlsdottir, R. & Huenges, E., 2005. The role of electrical interface conduction in geothermal exploration, *Proceedings World Geothermal Congress,* Antalya, Turkey, **0742,** 9.

Frisken, W.R., 1971. Extended industrial revolution and climate change, *EOS,* **52**(7), 500–508.

Fulignati, P., 2020. Clay minerals in hydrothermal systems, *Minerals,* **10,** 919.

Ghorbani, A., Revil, A., Coperey, A., Soueid, A.A., Roque, S., Heap, M.J., Grandis, H. & Viveiros, F., 2018. Complex conductivity of volcanic rocks and the geophysical mapping of alteration in volcanoes, *J. Volc. Geotherm. Res.,* **357,** 106–127.

Girdler, R.W., Fairhead, J.D., Searle, R.C. & Sowerbutts, W.T.C., 1969. Evolution of Rifting in Africa, *Nature,* **224**(5225), 1178–1182.

Glaser, D.R., 2021. A site-specific comparison of permeability prediction models in alluvial sediments from physical and geoelectrical measurements, *J. Environ. Eng. Geophys.,* **26,** 315–322.

Glaser, D.R., Barrowes, B.E., Shubitidze, F. & Slater, L.D., 2023. Laboratory investigation of high-frequency electromagnetic induction measurements for macro-scale relaxation signatures, *Geophys. J. Int.,* **235**(2), 1274–1291.

Glaser, D.R., Burch, K., Brinkley, D.L. & Reppert, P., 2021. Localization of deep voids through geophysical signatures of secondary dewatering features, *Geophysics,* **86,** WA139–WA152.

Gresse, M., Uyeshima, M., Koyama, T., Hase, H., Aizawa, K., Yamaya, Y. & Hata, M., 2021. Hydrothermal and magmatic system of a volcanic island inferred from magnetotellurics, seismicity, self-potential, and thermal image: an example of Miyakejima (Japan), *J. Geophys. Res. Solid Earth,* **126**(6), e2021JB022034, doi:10.1029/2021JB022034.

Günther, T. & Martin, T., 2016. Spectral two-dimensional inversion of frequency domain induced polarization data from a mining slag heap, *J. Appl. Geophys.,* **135,** 436–448.

Gurin, G., Titov, K. & Ilyin, Y., 2019. Induced polarization of rocks containing metallic particles: evidence of passivation effect, *Geophys. Res. Lett.,* **46,** 670–677.

Gurin, G., Titov, K., Ilyin, Y. & Tarasov, A., 2015. Induced polarization of disseminated electronically conductive minerals: a semi-empirical model, *Geophys. J. Int.,* **200**(3), 1555–1565.

Halisch, M., Weller, A. & Kassab, M.A., 2014. Impedance spectroscopy on carbonates, *Inter. Symp. Soc. Core Analysts,* paper *SCA2014-039*.

Hancock, C., Altunel, E. & Çakır, E., 1999. Travitonics: using travertines in active fault studies, *J. Struct. Geol.,* **21,** 903–916.

Kampunzu, A.B., Bonhomme, M.G. & Kanika, M., 1998, Geochronology of volcanic rocks and evolution of the Cenozoic Western Branch of the East African Rift System, *J. Afr. Earth Sci.,* **26,** 441–461.

Koohbor, B., Deparis, J., Leroy, P., Ataie-Ashtiani, B., Davarzani, H. & Colombano, S., 2022, DNAPL flow and complex electrical resistivity evolution in saturated porous media: a coupled numerical simulation, *J. Contam. Hydrol.,* **248,** 104 003, doi:10.1016/j.jconhyd.2022.104003.

Lesmes, D.P. & Frye, K.M., 2001. The influence of pore fluid chemistry on the complex conductivity and induced-polarization responses of Berea Sandstone, *J. geophys. Res.,* **106**(B3), 4079–4090.

Li, K., Pan, B. & Horne, R., 2025. Evaluating fractures in rocks from geothermal reservoirs using resistivity at different frequencies, *Energy,* **93**(1), 1230–1238.

Loke, M.H. & Barker, R.D., 1996. Practical techniques for 3D resistivity surveys and data inversion, *Geophys. Prospect.,* **44,** 499–523.

Ma, X., Schwartz, N., Chao, C., Li, J., Xia, T., Furman, A. & Mao, D., 2025. Unveiling spectral induced polarization responses of ZVI-AC-sand mixtures in groundwater remediation, *J. Geophys. Res. Solid Earth,* **130,** e2024JB030107, doi:10.1029/2024JB030107.

Martin, T., 2012. Complex resistivity measurements on oak, *Eur. J. Wood Wood Prod.,* **70,** 45–53.

Martin, T., Gunther, T., Flores Orozco, A. & Dahlin, T., 2020. Evaluation of spectral induced polarization field measurements in time and frequency domain, *J. Appl. Geophys.,* **180,** 104 141, doi:10.1016/j.jappgeo.2020.104141.

Martin, T., Nordsiek, S. & Weller, A., 2015. Low-frequency impedance spectroscopy of wood, *J. Res. Spectrosc.,* 910 447, doi:10.5171/2015.910447.

Mellage, A., Holmes, A.B., Linley, S., Vallée, L., Rezanezhad, F., Thomson, N., Gu, F. & Cappellen, P.V., 2018. Sensing coated iron-oxide nanoparticles with spectral induced polarization (SIP): experiments in natural sand packed flow-through columns, *Environ. Sci. Technol.,* **52**(24), 14 256–14 265.

Michon, L., Famin, V. & Quidelleur, X., 2022, Evolution of the East African Rift System from trap-scale to plate-scale rifting, *Earth Sci. Rev.,***231,** 104 089, doi:10.1016/j.earscirev.2022.104089.

Muñoz, G., 2014. Exploring for geothermal resources with electromagnetic methods, *Surv. Geophys.,* **35,** 101–122.

Muñoz, G., Bauer, K., Moeck, I., Schulze, A. & Ritter, O., 2010b. Exploring the Groß Schonebeck (Germany) geothermal site using a statistical joint interpretation of magnetotelluric and seismic tomography models, *Geothermics,* **39,** 35–45.

Muñoz, G., Ritter, O. & Moeck, I., 2010a. A target-oriented magnetotelluric inversion approach for characterizing the low enthalpy Groß Schönebeck geothermal reservoir, *Geophys. J. Int.,* **183,** 1199–1215.

Navelot, V., 2018. Petrophysical properties of volcanic rocks and impacts of hydrothermal alteration in the Guadeloupe Archipelago (West Indies), *J. Volc. Geotherm. Res.,* **360,** 1–21.

Nkinyam, C.M., Ujah, C.O., Asadu, C.O. & Kallon, D.V.V., 2025. Exploring geothermal energy as a sustainable source of energy: a systemic review, *Unconventional Res.,* **6,** 100 149, doi:10.1016/j.uncres.2025.100149.

Ntarlagiannis, D., Doherty, R. & Williams, K., 2010. Spectral induced polarization signatures of abiotic FeS precipitation, *Geophysics,* **75,** F127–F133.

Olhoeft, G.R., 1981a. Electrical properties of granite with implications for the lower crust, *J. geophys. Res.,* **86**(B2), 931–936.

Olhoeft, G.R., 1981b. Electrical properties of rocks, in *Physical Properties Rocks & Minerals,* pp. 257–297, eds, Touloukian, Y. S., Judd, W. R. & Roy, R. F., McGraw Hill.

Panwar, N., 2021. Induced polarization of carbonates, *J. Geophys. Res. Solid Earth,* **126,** e2021JB022029, doi:10.1029/2021JB022029.

Pasteels, P., Villeneuve, M., Paepe, P. & Klerkx, J., 1989. Timing of the volcanism of the southern Kivu province: implications for the evolution of the western branch of the East African Rift system, *Earth Planet. Sci. Lett.,* **94,** 353–363.

Pereira, M.L., Zanon, V., Fernandes, I., Pappalardo, L. & Viveiros, F., 2024. Hydrothermal alteration and physical and mechanical properties of rocks in a volcanic environment: a review, *Earth Sci. Rev.,* **252,** 104 754, doi:10.1016/j.earscirev.2024.104754.

Piolat, L., 2025. Induced polarization of volcanic rocks. 8. The case of intrusive igneous rocks, *Geophys. J. Int.,* **241,** 1348–1372.

Piolat, L., Géraud, Y. & Revil, A., 2023. Induced polarization images the plumbing system of hydrothermal vents in an Intracontinental Rift, Lake Abhé, Republic of Djibouti, *Geophys. Res. Lett.,* **50,** doi:10.1029/2023GL105145.

Pouclet, A., Bellon, H. & Bram, K., 2016. The Cenozoic volcanism in the Kivu rift: assessment of the tectonic setting, geochemistry, and geochronology of the volcanic activity in the South-Kivu and Virunga regions, *J. Afr. Earth Sci.,* **121,** 219–246.

Revil, A. & Gresse, M., 2021. Induced polarization as a tool to assess alteration in geothermal systems: a review, *Minerals,* **11,** 962, doi:10.3390/min11090962.

Revil, A. & Skold, M., 2011. Salinity dependence of spectral induced polarization in sands and sandstones, *Geophys. J. Int.,* **187,** 813–824.

Revil, A., 2012. Spectral induced polarization of shaly sands: influence of the electrical double layer, *Water Resour. Res.,* **48,** W02517, doi:10.1029/2011WR011260.

Revil, A., 2013. On charge accumulations in heterogeneous porous materials under the influence of an electrical field, *Geophysics,* **78**(4), D271–D291.

Revil, A., 2022, Induced polarization images alteration in stratovolcanoes, *J. Volc. Geotherm. Res.,* **429,** 107– 598.

Revil, A., Florsch, N. & Mao, D., 2015a. Induced polarization response of porous media with metallic particles—Part 1: a theory for disseminated semiconductors, *Geophysics,* **80**(5), D525–D538.

Revil, A., Abdel Aal, G.Z., Atekwana, E.A., Mao, D. & Florsch, N., 2015b. Induced polarization response of porous media with metallic particles—Part 2. Comparison with a broad database of experimental data, *Geophysics,* **80**(5), D539–D552.

Revil, A., Cathles, L.M., Losh, S. & Nunn, J.A., 1998. Electrical conductivity in shaly sands with geophysical applications, *J. geophys. Res.,* **103,** 23 925–23 936.

Revil, A., Eppehimer, J.D., Skold, M., Karaoulis, M., Godinez, L. & Prasad, M., 2013. Low-frequency complex conductivity of sandy and clayey materials, *J. Colloid Interface Sci.,* **398,** 193–209.

Revil, A., Le Breton, M., Niu, Q., Wallin, E., Haskins, E. & Thomas, D.M., 2017a. Induced polarization of volcanic rocks –1. Surface versus quadrature conductivity, *Geophys. J. Int.,* **208,** 826–844.

Revil, A., *et al.* 2017b. Complex conductivity of soils, *Water Resour. Res.,* **53**(8), 7121–7147.

Revil, A., Qi, Y., Ghorbani, A., Coperey, A., Soueid, A.A., Finizola, A. & Ricci, T., 2019. Induced polarization of volcanic rocks. 3. Imaging clay cap properties in geothermal fields, *Geophys. J. Int.,* **218,** 2, 1398–1427.

Revil, A., Qi, Y., Ghorbani, A., Gresse, M. & Thomas, D.M., 2021. Induced polarization of volcanic rocks. 5. Imaging the temperature field of shield volcanoes, *Geophys. J. Int.,* **225,** 1492–1509.

Revil, A., Soueid, A.A., Coperey, A., Ravanel, L., Sharma, R. & Panwar, N., 2020. Induced polarization as a tool to characterize shallow landslides, *J. Hydrol.,* **589,** 125 369, doi:10.1016/j.jhydrol.2020.125369.

Rwandan Republic Natural Resources Ministry, 1981. Lithological map of Rwanda.

Schiermeier, Q., 2013. Renewable power: Germany's energy gamble, *Nature,* **496**(7444), 156–158.

Sunguti, A.E., Muhizi, T., Kibet, J.K. & Kinyanjui, T.K., 2024. Geochemical Survey of the Nyamyumba and Bugarama Hot Springs in the Western Province of Rwanda, *Eur. J. Chem.,* **15,** 31–38.

Titov, K., Abramov, V., Emelianov, V. & Revil, A., 2024. Induced polarization of volcanic rocks. Part 7. Kimberlites, *Geophysical Journal International,* **236,** 233–248.

Villeneuve, M. & Chorowicz, J., 2004. Les sillons plissés du Burundien supérieur dans la chaîne Kibarienne d'Afrique centrale, *C.R. Geosci.,* **336,** 9, 807–814.

Villeneuve, M., 1978. La stratigraphie du précambrien au sud du lac Kivu (Zaïre oriental), *Bulletin de la Société Géologique de France,* **S7-XX**(6), 915–920.

Villeneuve, M., Gärtner, A., Buzera, C., Wazi, N.R., Zieger-Hofmann, M. & Linnemann, U., 2019. U-Pb ages and provenance of detrital zircon from metasedimentary rocks of the Nya-Ngezie and Bugarama groups (D.R. Congo): a key for the evolution of the Mesoproterozoic Kibaran-Burundian Orogen in Central Africa, *Precambrian Res.,* **328,** 81–98.

Vinegar, H.J. & Waxman, M.H., 1984. Induced polarization of shaly sands, *Geophysics,* **49,** 1267–1287.

Walter, B., Géraud, Y., Hautevelle, Y., Diraison, M. & Raisson, F., 2019. Fluid circulations at structural intersections through the Toro-Bunyoro fault system (Albertine rift, Uganda): a multidisciplinary study of a composite hydrogeological system, *Geofluids,* 8161469, doi:10.1155/2019/8161469.

Waxman, M.H. & Smits, L., 1968. Electrical conductivities in oil-bearing shaly sands, *Soc. Petrol. Eng. J.,* **8**(2), 107–122.

Weller, A. & Slater, L., 2015. Induced polarization dependence on pore space geometry: empirical observations and mechanistic predictions, *J. Appl. Geophys.,* **123,** 310–315.

Weller, A., Breede, K., Slater, L. & Nordsiek, S., 2011. Effect of changing water salinity on complex conductivity spectra of sandstones, *Geophysics,* **76**(5), F315–F327.

Weller, A., Seichter, M. & Kampke, A., 1996. Induced-polarization modelling using complex electrical conductivities, *Geophys. J. Int.,* **127,** 387–398.

Wong, J., 1979. An electrochemical model of the induced polarization phenomenon in disseminated sulfide ores, *Geophysics,* **44,** 1245–1265

Zhang, K., Chibati, N., Revil, A., Richard, J., Gresse, M., Xue, Y. & Géraud, Y., 2023, Induced polarization of volcanic rocks. 6. Relationships with other petrophysical properties, *Geophys. J. Int.,* **234,** 2375–2393.